(12) INTERNATIONAL APPLICATION PUBLISHED UNDER THE PATENT COOPERATION TREATY (PCT)

(19) World Intellectual Property Organization
International Bureau

(43) International Publication Date
26 February 2004 (26.02.2004)

PCT

(10) International Publication Number
WO 2004/016166 A1

(51) International Patent Classification[7]: A61B 5/05

(21) International Application Number: PCT/US2003/025396

(22) International Filing Date: 14 August 2003 (14.08.2003)

(25) Filing Language: English

(26) Publication Language: English

(30) Priority Data:
60/403,527 15 August 2002 (15.08.2002) US

(71) Applicant *(for all designated States except US)*: **YALE UNIVERSITY** [US/US]; Office of Cooperative Research, 333 Cedar Street, SHM-I-210, New Haven, CT 06520-8079 (US).

(72) Inventors; and

(75) Inventors/Applicants *(for US only)*: **SINUSAS, Albert, J.** [US/US]; 490 Briarwood Drive, Guilford, CT 06437 (US). **ZHU, Quing** [CN/US]; 22 Machele Lane, Mansfield, CT 06250 (US). **SADEGHI, Mehran, M.** [CA/US]; 1117 Aspen Glen Drive, Hamden, CT 06518 (US).

(74) Agent: **FLAXMAN, Howard, N.**; Welsh & Flaxman LLC, 2341 Jefferson Davis Highway, Suite 112, Arlington, VA 22202 (US).

(81) Designated States *(national)*: AE, AG, AL, AU, BA, BB, BR, BZ, CA, CN, CO, CR, CU, DM, DZ, EC, GD, GE, HR, ID, IL, IN, IS, JP, KP, KR, LC, LK, LR, LT, LV, MA, MG, MK, MN, MX, NI, NO, NZ, OM, PG, PH, PL, SC, SG, SY, TN, TT, UA, US, UZ, VC, VN, YU, ZA.

(84) Designated States *(regional)*: ARIPO patent (GH, GM, KE, LS, MW, MZ, SD, SL, SZ, TZ, UG, ZM, ZW), Eurasian patent (AM, AZ, BY, KG, KZ, MD, RU, TJ, TM), European patent (AT, BE, BG, CH, CY, CZ, DE, DK, EE, ES, FI, FR, GB, GR, HU, IE, IT, LU, MC, NL, PT, RO, SE, SI, SK, TR), OAPI patent (BF, BJ, CF, CG, CI, CM, GA, GN, GQ, GW, ML, MR, NE, SN, TD, TG).

Published:
— *with international search report*

[Continued on next page]

(54) Title: HYBRID OCT/SCINTIGRAPHY INTRAVASCULAR DEVICE

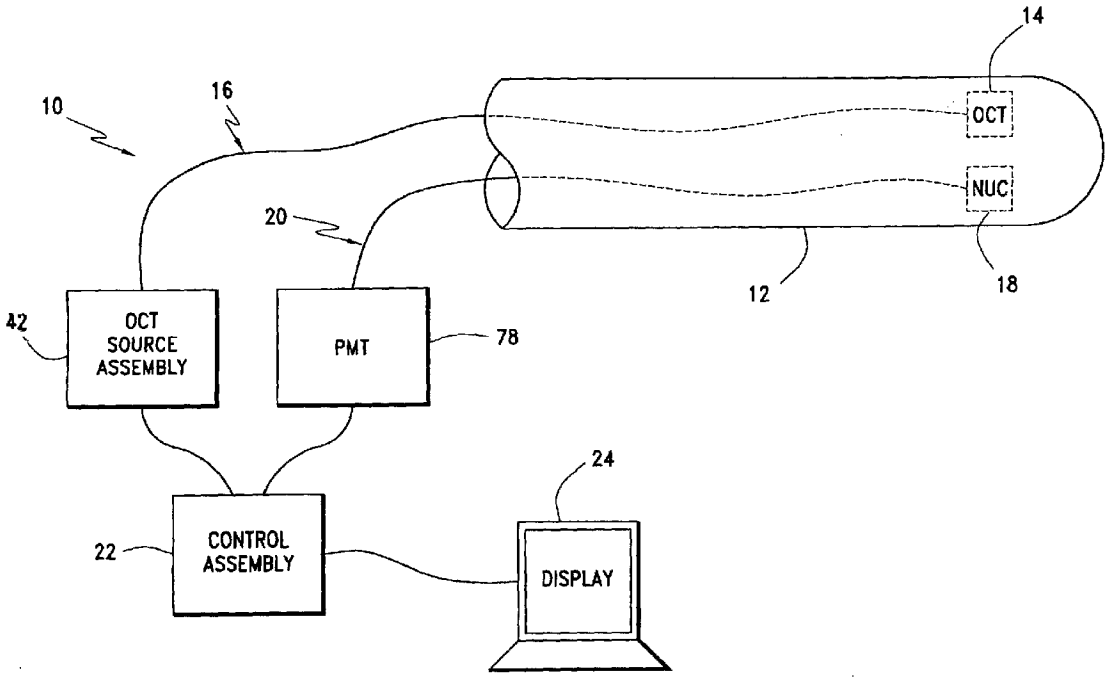

(57) Abstract: An imaging device includes a delivery device shaped and dimensioned for accessing a predetermined body cavity or lumen, an OCT system linked to the delivery device and a nuclear imaging system linked to the delivery device. The imaging device further includes a control assembly linked to the OCT system and the nuclear imaging system. The control assembly includes processing means adapted for gathering information from the OCT system and the nuclear imaging system and creating imaging information used in the assessment of the body cavity or lumen into which the delivery device is placed.

WO 2004/016166 A1

— *before the expiration of the time limit for amending the claims and to be republished in the event of receipt of amendments*

For two-letter codes and other abbreviations, refer to the "Guidance Notes on Codes and Abbreviations" appearing at the beginning of each regular issue of the PCT Gazette.

TITLE: HYBRID OCT/SCINTIGRAPHY INTRAVASCULAR DEVICE.

BACKGROUND OF THE INVENTION

1. Field of the Invention

The invention relates to an imaging device for use within body cavities and/or lumens. More particularly, the invention relates to an imaging device combining OCT with nuclear imaging based scintigraphy to optimize imaging within body cavities and/or lumens.

2. Description of the Prior Art

Coronary artery disease is the major cause of morbidity and mortality in the industrialized world. The major players in this morbidity and mortality are acute coronary syndromes (unstable angina and myocardial infarction), where rupture or erosion of the fibrous cap of a vulnerable atherosclerotic plaque leads to thrombus formation and occlusion of the blood vessel. Despite remarkable progress in treating coronary artery disease, we are still unable to predict which individual patient is prone to develop unstable coronary syndromes. Based on post-mortem studies, vulnerable plaques are morphologically defined as those with high lipid content, a small number of smooth muscle cells, an inflammatory infiltrate and a thin fibrous cap. Arbustini E, Dal Bello B, Morbini P, Burke AP, Bocciarelli M, Specchia G, et al. "Plaque Erosion Is A Major Substrate For Coronary Thrombosis In Acute Myocardial Infarction," Heart, 82:269-72, 1999; P. Libby, "Molecular Bases Of The Acute Coronary Syndromes," Circulation, 91(11): 2844-2850, 1995. There are currently no reliable non-invasive or invasive methods for the detection of these plaques in living subjects.

The arterial wall consists of three layers. Intima, normally only a single cellular layer thick, forms the inner layer surrounding the arterial lumen. It is separated from the middle layer, media, by an internal elastic membrane. In muscular arteries (like coronary arteries), the media mainly consists of smooth muscle cells and extracellular matrix. Adventitia, the outer layer, is separated from the media by an external elastic membrane. As the most common vascular pathologies are associated

with changes in the composition and structure of these layers, there is great interest in high-resolution imaging of the vessel wall. Diagnostic information obtained from such imaging techniques may greatly affect the management of cardiovascular diseases.

Presently, the only widely available diagnostic technique for assessing the vascular wall structure in vivo is intravascular ultrasound. Current clinical applications of imaging the (anatomical) composition of vessel walls include the determination of stenosis in angiographically intermediate lesions, where "lumenography" may not clearly reflect the extent of atherosclerotic burden. Another widely used application of intravascular ultrasound is to determine the accuracy of stent placement after balloon angioplasty.

Despite positive remodeling (increase in external vessel diameter), up to 40% of balloon angioplasties are followed by re-narrowing of arteries (restenosis), which is due to the formation of a thick intimal layer (neointima formation). Neointima formation can be seen in a number of other pathological states, such as diabetic coronary artery disease and chronic graft rejection after cardiac transplantation. Although helpful in the diagnosis of these processes, the usefulness of intravascular ultrasound is limited by its relatively limited resolution. As such, it is often difficult to clearly distinguish between different layers of vascular walls and to clearly demarcate their borders.

In muscular arteries, such as coronary arteries, the intima is relatively echogenic compared to the lumen and media. The trailing edge of intima (that would correspond to the internal elastic membrane) cannot always be distinguished clearly. Media is usually less echogenic than the intima. In some cases the media may appear artifactually thin because of "blooming," an intense reflection from the intima or external elastic membrane. In other cases, the media can appear artifactually thick because of signal attenuation and the weak reflectivity of the internal elastic membrane. In elastic arteries, such as the carotid artery, the media is more echo-reflective because of the higher elastin content. Mintz GS, Nissen SE, Anderson WD, Bailey SR, Erbel R, Fitzgerald PJ, Pinto FJ, Rosenfield K, Siegel RJ, Tuzcu EM,

Yock PG, ACC Clinical Expert Consensus Document On Standards For The Acquisition, Measurement And Reporting Of Intravascular Ultrasound Studies: A Report Of The American College Of Cardiology Task Force On Clinical Expert Consensus Documents
(Committee To Develop A Clinical Expert Consensus Document On Standards For Acquisition, Measurement And Reporting Of Intravascular Ultrasound Studies [IVUS]), J Am Coll Cardiol, 37:1478-92, 2001.

Although of some help in defining the anatomy of the plaque, intravascular ultrasound usually lacks the necessary resolution for fine definition of plaque structure. Optical coherent tomography (OCT) can reveal structures within the body to several millimeters in depth with unprecedented resolution on the order of 5 to 15 microns, which is an order of magnitude higher than intravascular ultrasound. D. Huang, E.A. Swanson, C.P. Lin, J.S. Schuman, W.G. Stinson, W. Chang, M.R. Hee, T. Flotte, K. Gregory, C.A. Puliafito, and J.G. Fujimoto, "Optical Coherence Tomography," Science, Vol. 254, 1178-1181, 1991; Rollins A., Sivak M.Jr., Radhakrishnan Sunita, Lass J. H., Huang David, Cooper K. D., Izatt J., "Emerging Clinical Applications Of Optical Coherent Tomogaphy," Optics and Photonics News, 37-41, April 2002; Rashed H, Izatt J, Toth C., "Optical Coherent Tomography Of The Retina," Optics and Photonics News, 48-51, April 2002; M. Brezinski and J. Fujimoto, "Imaging The Cardiovascular System With Optical Coherence Tomography," Optics and Photonics News, 34-35, April 2002; P. Patwari, N. Weissman, S. Boppart, C. Jesser, D. Stamper, J. G. Fujimoto and M. E. Brezinki, "Assessment Of Coronary Plaque With Optical Coherence Tomography And High-Frequency Ultrasound," The American Journal of Cardiology, 85: 641-644, 2000. Recent ex vivo studies have demonstrated that intravascular OCT can differentiate lipids from nonlipids and identify the intimal over the lipid collection. M. Brezinski and J. Fujimoto, "Imaging The Cardiovascular System With Optical Coherence Tomography," Optics and Photonics News, 34-35, April 2002; H. Yabushita, B. Bouma, S. Houser, H. Thomas, I. Jang, K. H. Schlendorf, C. R. Kauffman, M. Shishkov, D. Kang, E. F. Halpern, G. J. Tearney, "Characterization Of Human

Atherosclerosis By Optical Coherence Tomography," Circulation, 106(13): 1640-1653, 2002; IK Jang, BE Bouma, DH Kang, et al, "Visualization Of Coronary Artherosclerotic Plaques In Patients Using Optical Coherent Tomography: Comparison With Intravascular Ultrasound," J. Am. Coll. Cardiol., Vol. 39(4), 604-609, 2002; G. J. Tearney, IK Jang, DH Kang, et al., "Porcine Coronary Imaging In Vivo By Optical Coherent Tomography," ACTA CARDIDL 55(4) 233-237, 2000; J. M. Schmitt, C. L. Petersen, E. Mont and R. Virmani, " Imaging And Characterization Of Coronary Lesions With Optical Coherent Tomography," Proceedings of IEEE International Symposium on Biomedical Imaging, 106-109, Washington D.C. , July 7-10, 2002. High resolution imaging of vessel walls by OCT has, therefore, the potential of opening exciting new directions in the diagnosis and management of coronary artery disease.

As described in U.S. Patent No. 6,445,944, OCT is an interferometric imaging technology. OCT achieves high depth resolution (about 2 μ m to 20 μ m) via a combination of the focal properties of the imaging optics and the coherence properties of the optical source. OCT provides nearly shot-noise-limited detection and thus high sensitivity (>140 dB).

OCT uses the reflected light to obtain a cross-sectional image of tissue adjacent the transparent sheath window. The depth of tissue scan using OCT is based on low coherence interferometry; and the lateral tissue scan is based on the rotation of an optical beam by either a rotating mirror or a mechanical motor. In accordance with a preferred embodiment of the present invention and as those skilled in the art will certainly appreciate, OCT uses an interferometer with reference arm scanning and a low coherence light source.

As such, the light emitted by the OCT system described above is processed in the following manner. First, a low coherence light source is directed onto a beam splitter to produce two beams, a sampling measurement beam and a reference beam.

The sampling beam hits and penetrates the tissue or material to be imaged, and then reflects (backscatters) from the tissue, carrying information about the reflecting points from the surface and the depth of the tissue. The light delivered to the reference arm hits a reference reflector, for example, a mirror or a diffraction grating, and reflects from the

reference reflector. The reference arm travels a given path length, such that the reference reflector either moves or is designed such that the reflection occurs at different distances from the beam splitting point and returns at a different point in time or in space, which actually represents the depth scanning. The amount of such movement represents the desirable depth of penetration of the tissue or object being imaged by the sampling arm. Where OCT is applied the depth of light penetration is typically 2 to 3 millimeters.

The output of the interferometer is the superposition of the electromagnetic fields from the reflected reference arm and the sampling arm reflected from the tissue or material being imaged. When the reflected arms meet, interference is observed only where the path lengths of the reference arm and sampling arm are matched to within the coherence length of the light source. A photodetector detects this interference and converts it into electrical signals. The signals are electronically processed and ultimately displayed, for example, on a computer screen or other monitors.

Each cross-sectional image involves two scans: depth (axial) and width (lateral). Typically, the rate of depth scan is faster than the rate of lateral scan, as 200 to 300 or more depth scans may occur for one lateral scan during live imaging. A typical rate of lateral scanning during live imaging is approximately 26-30 scans per second. A typical OCT probe for linear cross sectional imaging uses a mechanical scanning arrangement in which at least one mechanical part reciprocates to create a scanning motion.

OCT detects reflected light and provides high-resolution imaging of intravascular structures, however, it has limited functional imaging capability. Recent research activities on improving OCT functional imaging capabilities include polarization sensitive OCT, Doppler blood flow OCT, contrast enhanced OCT, spectroscopy OCT, etc. Z. P. Chen, T.E. Milner, S. Srinivas, X.J. Wang, A. Malekafzali, M.J.C. van Germert, and J. S. Nelson, "Noninvasive Imaging Of *In Vivo* Blood Flow Velocity Using Optical Doppler Tomography," Optics Letters, Vol. 22, No. 14, pp. 1119-1121, July, 1997; J.A. Izatt, M.D. Kulkarni, S. Yazdanfar, J.K. Barton and A.J. Welch, "*In Vivo* Bi-Directional Color Doppler Flow Imaging Of Picoliter Blood Volumes Using Optical Coherence Tomography," Optics Letters,

Vol. 22, No. 18, pp. 1439-1441, September, 1997; T.G. van Leeuwen, M.D. Kulkarni, S. Yazdanfar, A.M. Rollins, and J.A. Izatt, "High-Flow-Velocity And Shear-Rate Imaging By Use Of Color Doppler Optical Coherence Tomography," Optics Letters, Vol. 24, No. 22, pp. 1584-1586, November, 1999; DQ. Piao, N. Datta, L. Otis, Q. Zhu, "Quantitative Assessment Of Flow Velocity Estimation Algorithms For Optical Doppler Tomography Imaging," Applied Optics, 41 (29): 6118-6127, 2002; DQ. Piao, L. Otis, and Q. Zhu, "Doppler Angle And Flow Velocity Mapping By Combining Doppler Shift And Doppler Bandwidth Measurements In Optical Doppler Tomography," Optics Letters, in press; F. J-J Toublan, et al, "Magnetically-Induced Optical Contrast Agents For Optical Coherent Tomography," OSA Biomedical Topical Meeting, 257-262, 2002; M. Pierce, B. H. Park, B. Cense and J. F. de Boer, "Simultaneous Intensity, Birefringence, And Flow Measurements With High-Speed Fiber-Based Optical Coherent Tomography," Optics Letters, 27(17) 1534-1536, 2002; C. E. Saxer, J. F. de Bore, B. H. Park, Y. Zhao, Z. Chen and J. S. Nelson, "High-Speed Fiber-Based Polarization-Sensitive Optical Coherent Tomograpy Of In Vivo Human Skin," Optics Letters, 25, 1355-1357,2000; A. Jiao and L. V. Wang, "Two-Dimensional Depth-Resolved Muellaer Matrix Of Biological Tissue Measured With Double-Beam Polarization-Sensitive Optical Coherence Tomography," Optics Letters, Vol. 27 (2), 2002; K. D. Rao, M. A. Choma, S. Yazdanfar, A. Rollins and J. Izatt, "Molecular Contrast In Optical Coherent Tomography By Use Of A Pump-Probe Technique," Optics Letters, Vol. 28, No.28, 341-344, 2003; J. M. Schmitt, S. H. Xiang, and K. M. Yuang, "Differential Absorption Imaging With Optical Coherent Tomography," J. Opt. Soc. Am. A Vol. 15, No.9, 2288-2296, 1998.

Conventional approaches for imaging of atherosclerosis with single photon emission computed tomographic (SPECT) and Positron Emission Tomography (PET), while feasible, provide limited image resolution and/or sensitivity to fully characterize targeted radiolabeled tracers. Therefore, a number of investigators are developing intravascular radiation detection systems for early detection of atherosclerosis. B. E. Patt, J. S. Iwanczyk, L. MacDonald, Y. Yamaguchi, C. Tull,

"Intravascular Probe For Detection Of Vulnerable Plaque," Proceedings of SPIE, Vol. 4508, 88-98, 2001; Lederman RJ. Raylman RR. Fisher SJ. Kison PV. San H. Nabel EG. Wahl RL., "Detection Of Atherosclerosis Using A Novel Positron-Sensitive Probe And 18-Fluorodeoxyglucose (FDG)," Nuclear Medicine Communications. 22(7):747-53, 2001; Raylman RR. Wahl RL, et al., "A Fiber-Optically Coupled Positron-Sensitive Surgical Probe," Journal of Nuclear Medicine, 35(5):909-13, 1994; M. P. Tornai, G. S. Levin, L. R. MacDonald , C. H. Holdsworth E. J. Hoffman, "A Miniature Phoswitch Detector For Gamma-Ray Localization And Beta Imaging," IEEE Transactions on Nuclear Science, 45(3): 1166-1173, 1998; EJ Hoffman, MP Tornai, CS Levin, "Gamma And Beta Intra-Operative Probes," Nucl. Instr. Meth. A389:324:329, 1997.

Nuclear imaging based scintigraphy systems function in the following manner. In practice, injected radioactive agents are targeted to the organ under study. Depending upon the body vessel or cavity being studied, various radioactive agents may be employed so as to produce the highest resolution and signal to background noise image of the vessel or cavity being studied. As those skilled in the art will certainly appreciate, the radiation emitted by the radioactive agents bombards the scintillation fibers, producing a signal (such as light) within the scintillation fibers. The resulting signals are transmitted to the opposite ends of the respective scintillation fibers. The signals are inputted in the signal-receiving elements. The light pulses are then converted into electrical signals and are inputted into a time-to-amplitude converter through constant-fraction discriminators, and a signal delay circuit. The time-to-amplitude converter outputs an electrical pulse to create a pulse height in proportion to the time difference between the time periods required for the light pulses to reach the respective light detectors. The pulse from the time-to-amplitude converter is inputted into the analog-digital converter.

Although more than one radiation can be incident on the scintillation fiber, it is possible to see the incident positions of the radiations by discriminating the pulse-heights of the electrical pulses at the multichannel pulse-height analyzer, and to detect a radiation dose-rate based on count.

Compared with external imaging, intravascular approaches have the significant advantage of detecting localized small lesions that might involve the endothelial cells or the underlying structures. Even an ideal radiolabeled agent for atherosclerosis imaging might deliver only ~0.01% of the administered dose to the target lesion. B. E. Patt, J. S. Iwanczyk, L. MacDonald, Y. Yamaguchi, C. Tull, "Intravascular Probe For Detection Of Vulnerable Plaque," Proceedings of SPIE, Vol. 4508, 88-98, 2001. These intravascular systems offer improved sensitivity for detection of small amounts of radioactivity, although spatial resolution is limited.

While several groups have been developing an intravascular radiation detector, the prior art has so far failed to compensate for intravascular radiation detection devices inability to provide for simultaneous high-resolution imaging of structure. Since most vascular lesions are associated with changes in the composition and structure of the vessel wall, there is great need for such high-resolution imaging of the vessel wall.

Studies have shown that vulnerable plaques are metabolically active and can be detected at an early stage if the endothelium or underlying media is directly interrogated. B. E. Patt, J. S. Iwanczyk, L. MacDonald, Y. Yamaguchi, C. Tull, "Intravascular Probe For Detection Of Vulnerable Plaque," Proceedings of SPIE, Vol. 4508, 88-98, 2001. One of the most effective metabolic tracers in the injured rabbit aorta model employed to screen radiopharmaceuticals is Fluorodeoxyglucose (FDG) labeled with ^{18}F positron (beta) radionuclide emitter. Lederman RJ. Raylman RR. Fisher SJ. Kison PV. San H. Nabel EG. Wahl RL., "Detection Of Atherosclerosis Using A Novel Positron-Sensitive Probe And 18-Fluorodeoxyglucose (FDG)," Nuclear Medicine Communications. 22(7):747-53, 2001. The half-life (110 min) of ^{18}F is relatively long compared to other positron emission tracers. FDG accumulation appears to correspond to regions of subintimal cellular infiltration. FDG uptake is one marker of the relative hypermetabolic state of atherosclerotic tissue, which is characterized by a dense cellular infiltration of macrophages and lymphocytes.

Most catheter-based radiotracer detection systems have focused on beta detection of positron emitting tracers using scintillating plastic fibers. Since the targeted cardiac vessels have diameters of less than 5 mm, they correspond well with the tissue path length (~3 mm) for beta particles with energies of >600 keV. The catheter designed by Patt et al. employs 0.5 mm diameter scintillating fibers. B. E. Patt, J. S. Iwanczyk, L. MacDonald, Y. Yamaguchi, C. Tull, "Intravascular Probe For Detection Of Vulnerable Plaque," Proceedings of SPIE, Vol. 4508, 88-98, 2001. This system has demonstrated acceptable sensitivity for detection of ^{18}F of >400 cps/uCi at 1mm from the detector. ^{18}F labeled tracers have been developed for other targets such as the alpha-v beta-3 integrin, which may be upregulated in the unstable plaque. The detection of the unstable or vulnerable atherosclerotic plaque may be enhanced by more specific vascular markers, like the alpha-v beta-3 integrin. The catheter-based scintillating probes provide limited spatial resolution and can, at most, identify activities about the size of catheter tips (approximately several mms).

With the foregoing in mind, it is apparent a need exists for a system capable of overcoming the individual shortcomings of scintillating probes and OCT. The present invention provides a novel hybrid catheter-based device, which integrates an OCT probe and scintillating fibers for dual-modality high-resolution structural and high-contrast functional imaging of coronary diseases, using ^{18}F labeled tracers. The development of the present device will open an exciting new research direction for high-resolution molecular imaging of vascular, and other intra-cavity diseases.

SUMMARY OF THE INVENTION

It is, therefore, an object of the present invention to provide an imaging device including a delivery device shaped and dimensioned for accessing a predetermined body cavity or lumen, an OCT system linked to the delivery device and a nuclear imaging system linked to the delivery device.

It is also an object of the present invention to provide an imaging device including a control assembly linked to the OCT system and the nuclear imaging system. The control assembly includes processing means adapted for gathering information from the OCT system and the nuclear imaging system and creating imaging information used in the assessment of the body cavity or lumen into which the delivery device is placed.

It is another object of the present invention to provide an imaging device wherein the OCT system includes scanning components housed within the delivery device and an OCT source assembly remote from the delivery device.

It is a further object of the present invention to provide an imaging device wherein the scanning components of the OCT system include an optical fiber extending from the OCT source assembly through the length of the delivery device, a lens secured to a distal end of the optical fiber and a rotating right angle prism positioned for receiving light from the lens.

It is also another object of the present invention to provide an imaging device wherein rotation of the right angle prism is controlled by a motor coupled to the right angle prism.

It is still another object of the present invention to provide an imaging device wherein the motor is housed within a distal end of the delivery device.

It is also an object of the present invention to provide an imaging device wherein the motor is positioned adjacent a proximal end of the delivery device.

It is a further object of the present invention to provide an imaging device wherein the nuclear imaging system includes scintillating fibers positioned adjacent a distal end of the delivery device.

It is another object of the present invention to provide an imaging device wherein the scintillating fibers are sheathed in the area adjacent a proximal end of the delivery device.

It is also an object of the present invention to provide an imaging device wherein two to six scintillating fibers are positioned adjacent the distal end of the delivery device.

It is yet a further object of the present invention to provide an imaging device wherein the scintillating fibers are coupled to a proximal end of the delivery device by optical fibers extending from the scintillating fibers to the proximal end of the delivery device.

It is another object of the present invention to provide a method for imaging body lumens or cavities. The method is achieved by first inserting a delivery device to a predetermined location within a body previously marked with radioactive markers. The delivery device includes an OCT system linked to the delivery device and a nuclear imaging system linked to the delivery device. The method further includes scanning the predetermined location with the OCT system for obtaining a high resolution image and sensing the radioactive markers with the nuclear imaging system to obtain a high contrast image of the predetermined location.

Other objects and advantages of the present invention will become apparent from the following detailed description when viewed in conjunction with the accompanying drawings, which set forth certain embodiments of the invention.

BRIEF DESCRIPTION OF THE DRAWINGS

Figure 1 is a schematic of the present imaging system.

Figure 2 is a schematic of a first embodiment in accordance with the present invention.

Figure 3 is a schematic of a second embodiment in accordance with the present invention.

Figure 4 is a schematic of the OCT source assembly.

Figure 5 is in vivo simultaneous structural and blood flow imaging of two clusters of the abdominal vessels of a small rat with pulsatile flow.

Figure 6 is a graph of detection sensitivity versus distance between radiation source and scintillating fiber tips.

Figure 7 is a graph of total counts v. lateral position of beta source relative to the scintillating fiber tips.

Figure 8 is an illustration of position sensitive PMT resistor network and multi-channel radiation detection system for spatial mapping.

Figure 9 is a schematic of a prototype in accordance with the present invention.

Figure 10 is a perspective view of the prototype shown in Figure 9.

Figure 11 is co-registered OCT images and positron detection simultaneously acquired from a fresh bovine coronary artery. The location of point source beta emitter is pointed by the white arrow.

Figure 12 is an OCT image showing the layered structure of the vessel of Figure 11.

Figure 13 is a schematic of a recirculation perfusion system.

DESCRIPTION OF THE PREFERRED EMBODIMENTS

The detailed embodiments of the present invention are disclosed herein. It should be understood, however, that the disclosed embodiments are merely exemplary of the invention, which may be embodied in various forms. Therefore, the details disclosed herein are not to be interpreted as limiting, but merely as the basis for the claims and as a basis for teaching one skilled in the art how to make and/or use the invention. Where alternate embodiments are described herein, the same reference numerals will be used in designating similar elements.

With reference to the accompanying figures, an imaging device 10 is disclosed. The imaging device is adapted for positioning within a predetermined body lumen and/or cavity and retrieving imaging information relating to the body lumen and/or cavity. The imaging device 10 provides a system capable of offering dual-modality high-resolution structural and high-contrast functional imaging of body lumens and/or cavities In accordance with a preferred embodiment of the present invention, the imaging device 10 is shaped, dimensioned and adapted for intravascular access for obtaining imaging information regarding the detection of unstable atherosclerotic plaque (coronary vessels, carotid vessels, renal vessels, peripheral vessels, etc.), the detection of restenosis following percutaneous angioplasty with or without stenting, the evaluation of brachytherapy following percutaneous angioplasty performed with coated stents or an intravascular radiation source and/or the evaluation of cardiac transplant vasculopathy.

While the present imaging device 10 is adapted for intravascular studies in accordance with a preferred embodiment of the present invention, it is contemplated the present imaging device 10 may be used as an endoscopic device with applications in the evaluation of gastrointestinal pathology. It is further contemplated the present imaging device 10 may be readily modified for use as a bronchoscopic device with applications in the evaluation of pulmonary pathology. It is still further contemplated the present imaging device 10 may be modified for use as an endoscopic device with applications in the detection of tumors in multiple organ systems (for example, gastrointestinal tract, pulmonary tract and/or other organ systems). Where the present imaging device 10 is adapted for other applications it may be linked with laparoscopic surgical techniques and interventions. In particular, the application of the present imaging device 10 to cancer detection will

foster new excitement in the early detection of cancer at the cellular level, which may lead to early detection and final eradication of some deadly diseases.

In accordance with a preferred embodiment of the present invention, and with reference to the alternate embodiments disclosed with reference to Figures 1, 2 and 3, the imaging device 10 includes a delivery device 12 shaped and dimensioned for accessing a predetermined body cavity or lumen. The scanning components 14 of an optical coherent tomography (OCT) system 16 and the sensing components 18 of a nuclear imaging system 20 are housed within the delivery device 12. The imaging device 10 further includes a control assembly 22 linked to the OCT system 16 and the nuclear imaging system 20. The control assembly 22 includes processing means adapted for gathering information from the OCT system 16 and the nuclear imaging system 20 for display on a monitor 24. The control assembly 22 further creates imaging information used in the assessment of the body cavity and/or lumen into which the delivery device 12 is placed.

Optical coherent tomography (OCT) is an imaging technique capable of providing subsurface high-resolution images on the order of 5 to 10 microns, which is an order of magnitude higher than conventional intravascular ultrasound. Nuclear imaging-based intravascular approaches, for example, nuclear imaging based scintigraphy, offer the significant advantage of detecting localized lesions labeled by highly specific radioactive tracers; that is, nuclear imaging approaches offer the ability to provide high contrast imaging of predetermined body vessels. In accordance with the present invention, high-resolution OCT imaging and high-contrast nuclear imaging are integrated for simultaneous structural imaging.

As discussed above, the delivery device 12 is preferably a catheter-based system adapted for intravascular access. As those skilled in the art will certainly appreciate, various catheter structures may be employed without departing from the spirit of the present invention. As will be described below in greater detail, the scanning components 14 of the OCT system 16 and the sensing components 18 of the nuclear imaging system 20 are positioned within the most distal 10-15 mm of the catheter 12. As such, the inclusion of the scanning components 14 of the OCT system 16 and the sensing components 18 of the nuclear imaging system 20 within the catheter 12 does not

substantially affect the flexibility of the catheter 12. The catheter 12 is, therefore, capable of insertion within deep and curved portions of vessels under study.

The catheters 12 utilized in accordance with the present invention must, however, include structural functionality adapted for supporting the scanning components 14 of the OCT system 16 and the nuclear imaging based scintigraphy system 20. In accordance with a preferred embodiment of the present invention, the catheter 12 is constructed with a diameter of approximately 2.0 mm, although those skilled in the art will certainly appreciate various constructions which may be utilized in accordance with the spirit of the present invention.

With reference to the alternate embodiments disclosed in Figures 2 and 3 (the same reference numerals are used for like components), and in accordance with preferred embodiments of the present invention, the scanning components 14 of the OCT system 16 housed within the catheter 12 generally include a single mode optical fiber 26, an ultrasonic micromotor 28 (see Figure 3) or a proximally positioned DC motor 30 (see Figure 2), a gradient index (GRIN) lens 32, a right angle prism 34 directed toward a transparent sheath window 36 formed in the catheter wall 38 and a rotor 40 powered by the ultrasonic micromotor 28 (see Figure 3).

More particularly, the single mode fiber 26 extends from an OCT source assembly 42 through the length of the catheter 12. The GRIN lens 32 is secured to the distal end 44 of the single mode fiber 26. The GRIN lens 32 receives light from the single mode fiber 26 and delivers light intravascularly via the tiny right angle prism 34. The right angle prism 34 is controlled for angular motion by a proximally positioned DC motor 30 (see Figure 2) or by a tiny micrometer 28 (see Figure 3). The light delivered to the prism 34 by the GRIN lens 32 is reflected 90 degrees relative to the longitudinal axis of the catheter 12 at its distal end. The reflected light is passed through the transparent sheath window 36 of the catheter 12 and onto the vascular wall. The prism 34 is then rotated under the control of the motor 28, 30 and the light reflected passes through the transparent sheath window 36 toward the surrounding tissue of the vessel. Since there is no rotation or bending driven by external forces involved in the proximal end of the catheter 12 and the solid part of the catheter is only 10-15 mm in the distal end, the catheter 12 is capable of insertion within deeper and curved vessels.

As shown with reference to Figures 2 and 3, two designs have been contemplated for the implementation of the scanning components of the OCT system 16 in accordance with the present invention. In accordance with a first embodiment, several groups have implemented OCT catheters for intravascular or gastrointestinal structural imaging. Bouma, M.E. Brezenski, N.J. Weissman, J.F. Southern, and J.G. Fujimoto, "Scanning Single-Mode Fiber Optical Catheter-Endoscope For Optical Coherence Tomography," Optics Letters, Vol. 21, No. 7, pp. 543-545, April, 1996; A. M. Rollins, R. Ung-arunyawee, A. Chark, R.C.K. Wong, K. Kobayashi, M.V. Sivak, Jr., and J.A. Izatt, "Real-Time *In Vivo* Imaging Of Human Gastrointestinal Ultrastructure By Use Of Endoscopic Optical Coherence Tomography With A Novel Efficient Interferometer Design," Optics Letters, Vol. 24, No. 19, pp. 1358-1360, October, 1999. Their catheter consists of a DC motor-gear assembly at the proximal end and a rotating shaft. The rotating shaft, which consists of a single-mode optical fiber and distal focusing elements of GRIN lens and right angle prism (or microprism), is driven by the gear assembly and can freely rotate inside the catheter sheath. The bending-induced fiber birefringence as the probe is manipulated within the body is compensated by a faraday rotator at the distal end. A. M. Rollins, R. Ung-arunyawee, A. Chark, R.C.K. Wong, K. Kobayashi, M.V. Sivak, Jr., and J.A. Izatt, "Real-Time *In Vivo* Imaging Of Human Gastrointestinal Ultrastructure By Use Of Endoscopic Optical Coherence Tomography With A Novel Efficient Interferometer Design," Optics Letters, Vol. 24, No. 19, pp. 1358-1360, October, 1999. We contemplate adopting this OCT scanning component design by integrating a single-mode optical fiber 26 and two to eight, preferably two to six, and particularly, four, scintillating fibers 46 inside a catheter 12 (see Figure 2). As will be discussed below in greater detail, the four scintillating fibers 46 improve the sensitivity as well as spatial mapping of radiation activities. Since the single-mode optical fiber 26 connected to the distal GRIN lens 32 and microprism 34 needs to be freely rotated inside the catheter while the scintillating fibers 46 are stationary, an inner sheath or a gap (not shown) is provided between single-mode optical fiber 26 and the scintillating fibers 46 to ensure free rotation of the scanning components 14.

In accordance with a second embodiment, and with reference to Figure 3, a tiny micromotor 28 is positioned at the distal end of the catheter 12. As with the embodiment described

above with reference to Figure 2, the micromotor 28 is coupled to the right angle prism 34 for control rotation. The basic principle of the ultrasonic motor can be found in S.S Lih, Y. Bar-Cohen, and W. Grandia, "Rotary Ultrasonic Motors Actuated By Traveling Flexural Waves," SPIE International Conference, Smart Structures and Materials Symposium, San Diego, CA, 3-6 March 1997. To our knowledge, the ultrasonic micromotors of this size are the smallest that can be made today. This size is small enough to fit into a regular endoscope's catheter.

The proximal end of the catheter 12 has a stationary single-mode fiber 26 and is glued to a GRIN lens 32 of approximately 1 mm in size (in accordance with a preferred embodiment the lens is manufactured by OZ Optics Inc.) for delivering light to a tiny right angle prism 34, which is attached to a rotating ultrasonic micromotor 28 positioned at the distal end of the catheter. The light delivered to the prism is reflected 90 degrees and focused inside the tissue. The speed of the smallest motors can go up to 2000 ~3000 rpm, which corresponds to more than 25 rotations per second. Since one rotation of the micromotor generates one frame of a B-scan OCT image, we can at least achieve 25 frames per second based on current available motor specifications.

This design does not require an inner sheath as is required with the first embodiment, because both optical fiber 26 and scintillating fibers 46 are stationary. However, the catheter sheath 38 must provide a rigid housing for the motor 28 since the micromotor 28 is positioned at the distal end. This is achieved by the provision of motor terminators 48. In addition, the GRIN lens 32, although separated from the motor assembly 28, must be housed rigidly as well to maintain stable light alignment and focusing.

The catheter 12 is made with biocompatible material, such as fused silica. In order to maintain a desired housing for the motor 28 and GRIN lens 32 while providing a transparent sheath window 36 to beta particle and OCT light, a rigid transparent plastic capillary tubing less than 10mm in length is positioned at the catheter 12 tip, and the micromotor assembly 28 plus GRIN lens 32 are glued inside the plastic capillary tubing 36 with optical cement.

In practice, the present OCT system 16 functions in the following manner. Light is applied to the single mode fiber 26. The transmitted light is passed through the GRIN lens 32 secured to the distal end 44 of the single mode fiber 26 and the light is ultimately delivered intravascularly via

the tiny right angle prism 34. The right angle prism 34 is controlled for angular motion by the micromotor 28 or the proximally positioned DC motor 30. The light delivered to the prism 34 by the GRIN lens 32 is reflected 90 degrees relative to the longitudinal axis of the catheter 12 at its distal end. The reflected light is passed through the transparent sheath window 36 of the catheter 12 and onto the vascular wall. The right angle prism 34 is then rotated under the control of the motor 28, 30 and the light reflected passes through the transparent sheath window 36 toward the surrounding tissue of the vessel. The light is then reflected back to the OCT system 16 and ultimately utilized in the creation of an image of the scanned vessel.

As such, and as those skilled in will appreciate, the light emitted by the OCT system 16 described above is processed in the following manner. First, a low coherence light source is directed onto a beam splitter to produce two beams, a sampling measurement beam and a reference beam. The sampling arm and the reference arm are then transmitted through the single mode fiber 26, the gradient index lens 32 and the right angle prism 34 where they are applied to the vessel tissue.

The sampling arm hits and penetrates the tissue or material to be imaged, and then reflects (backscatters) from the tissue, carrying information about the reflecting points from the surface and the depth of the tissue. The reference arm hits a reference reflector, for example, a mirror or a diffraction grating, and reflects from the reference reflector. The reference arm travels a given path length, such that the reference reflector either moves or is designed such that the reflection occurs at different distances from the beam splitting point and returns at a different point in time or in space, which actually represents the depth scanning. The amount of such movement represents the desirable depth of penetration of the tissue or object being imaged by the sampling beam. Where OCT is applied the depth of light penetration is typically 2 to 3 millimeters.

The output of the interferometer is the superposition of the electromagnetic fields from the reflected reference arm and the sampling arm reflected from the tissue or material being imaged. The output is gathered by the right angle prism 34 and transmitted through the single mode fiber 26 to the control assembly 22 where the information is processed to produce an image for viewing. When the reflected arms meet, interference is observed only where the path lengths of the reference arm and sampling arm are matched to within the coherence length of the light source. A

photodetector detects this interference and converts it into electrical signals. The signals are electronically processed and ultimately displayed, for example, on a computer screen or other monitor.

In accordance with a preferred embodiment of the present invention, the reference arm, sampling arm and reflected beams are generated and processed in the following manner. More particularly, and in accordance with a preferred embodiment of the present invention, two OCT source assemblies 42 have been developed for utilization in conjunction with the OCT system of the present invention. As those skilled in the art will certainly appreciate, the OCT source assembly 42 is positioned remote from the scanning components 14 and is linked to the scanning components 14 via the single mode fiber 26 described above. The respective source assemblies 42 are described in DQ. Piao, L. Otis, and Q. Zhu, "Doppler Angle And Flow Velocity Mapping By Combining Doppler Shift And Doppler Bandwidth Measurements In Optical Doppler Tomography," Optics Letters, (28) No.13., 1120-1123; Chen, NG and Zhu, Q, "Rotary Mirror Array for High Speed Optical Coherence Tomography," Optics Letters, (27) No.8., 607-609, April, 2002, which are incorporated herein by reference (copies attached hereto). In addition to the OCT source assemblies 42, a DSP real-time data processing unit, which can be used in conjunction with the present vascular imaging system, is also provided. In accordance with a preferred embodiment of the present invention, a DSP real-time data processing unit is disclosed in Yan, S., Piao, DQ, Chen Y., and Zhu Q, "A DSP-Based Real-Time Optical Doppler Tomography System," J. of BioOptics, submitted May, 2003, which is incorporated herein by reference (copy attached hereto).

In accordance with a preferred embodiment of the present invention, and with reference to Figure 4, the OCT source assembly 42 is a typical balanced setup configured with one 1×2 and one 2×2 fiber couplers 50, 52. The low coherence source is a superluminescent diode 54 with approximately 1310nm center wavelength, 60nm spectral width, and 10.0mW maximum output power. In the reference arm, a scanning optical delay line based on Littrow-mounting of diffraction grating 56 is used to generate range scanning and a phase modulation for carrier frequency as well. In the sample arm, a galvanometer 58 and achromatic lens pair 60, 61 are integrated to perform

repeatable lateral scanning, which is essential for the demonstration of continuous monitoring of structure imaging and blood flow.

In the detection arm, reflected light is transmitted through a glass capillary 74, a lens 76, 77 and galvanometer 72. The signal is detected differentially by an auto-dual balanced receiver 62, with which the source intensity noise is rejected. The signal is then amplified, bandpass filtered 64 and digitized using a computer 70. Using this system, one frame cross-sectional imaging per second is obtained by driving reference arm and sample arm galvanometers with approximately a 128 Hz triangle wave and a 1Hz saw tooth wave, respectively.

The imaging frame rate of an OCT source assembly 42 employing grating-based delay line is set by the galvanometer 72. For a frame rate of 8 frames/second, the galvanometer scanning speed is $f_g = 2048Hz$ assuming 256 A-lines per frame. At this scanning speed, the phase modulation is in the mega-hertz range. To facilitate this high speed scanning, a photo-receiver and filter having a broad bandwidth are needed. In accordance with a preferred embodiment of the grating-based OCT source assembly described above, the photo-receiver has a cutoff frequency of 125KHz, and the band-pass filter has maximum bandwidth of 102.4KHz. Limited by these two components, the current delay line cannot run at higher than 128Hz. As such, it is contemplated that the current photo-receiver and filter may be replaced with Newfocus 1817-FC photo-receiver and Frequency Devices 818 series filters to achieve 8 frames/second imaging frame rate.

With regard to the DSP real-time data processing unit and display unit, they provide for simultaneous tissue structure and blood flow imaging based on a custom designed digital signal processor (DSP) module. Yan, S., Piao, DQ, Chen Y., and Zhu Q, "A DSP-based real-time optical Doppler tomography system," J. of BioOptics, submitted May. 2003. The DSP is incorporated into the above-described OCT source assembly. Two advanced velocity estimation algorithms are embedded in this DSP module. Experiments on intralipid flow demonstrate that this DSP system is capable of imaging pulsatile flow at a rate of several hundred pulses per minute. *In vivo* real-time imaging capability of pulsatile blood flow in small rate is also demonstrated (see Figure 5).

In addition, and in accordance with a further embodiment of the OCT source assembly 42, a fast OCT source assembly 42 is provided for implementing a periodical modulation of the optical

path length in the reference arm. As mentioned above, this embodiment is disclosed in Chen, NG and Zhu, Q, "Rotary Mirror Array For High Speed Optical Coherence Tomography," Optics Letters, (27) No.8, 607-609, April, 2002, which is incorporated herein by reference. The fast OCT source assembly includes a linear delay line. The OCT source assembly 42 uses a regular motor of 4000 revolutions per minute (rpm). Up to 2400 A-lines were acquired every second in a 2 mm range, with less than 0.1% nonlinear effects. For a typical B-scan consisting of 256 A-scan lines, 8 frames/second have been achieved. A much higher scan rate up to 30 frames/second can be readily obtained by replacing our current motor with high-speed motors, e.g., 24,000-30,000 rpm.

As discussed above, nuclear imaging is combined with OCT in an effort to negate the deficiencies inherent in the use of OCT. In accordance with a preferred embodiment of the present invention, and with Reference to Figures 2 and 3, nuclear imaging is achieved through the utilization of scintillating fibers 46. However, it is contemplated other nuclear imaging techniques may be employed without departing from the spirit of the present invention.

In accordance with a preferred embodiment, the present imaging device 10 includes a plurality of scintillating fibers (four in accordance with a preferred embodiment of the present invention) distributed around an OCT single mode fiber 26 positioned in the center of the catheter 12. Four scintillating fibers 46 improve the sensitivity as well as spatial mapping of radiation activities. The four scintillating fibers 46 are approximately 0.5 mm in size and are designed to provide a coarse spatial resolution regarding the approximate size of detected radiation inside the vessel in which the present imaging device is utilized.

As those skilled in the art will certainly appreciate, scintillating fibers 46 of approximately 0.5 mm have been chosen in accordance with a preferred embodiment of the present invention and other sizes may be utilized depending upon required functionality without departing from the spirit of the present invention. In addition, four scintillating fibers 46 are employed in accordance with a preferred embodiment of the present invention, although two to eight fiber versions have been contemplated and those skilled in the art may certainly appreciate other fiber arrangements improving the positron detection sensitivity and spatial mapping without departing from the spirit of the present invention.

The scintillating fibers 46 extend the entire length of the catheter 12 and are ultimately connected to the control assembly 22 for transmission of the signal generated by radiation emitted within the body vessel or cavity. In order to accommodate the need for flexibility required by the present imaging device 10, the present invention employs the approach described in B. E. Patt, J. S. Iwanczyk, L. MacDonald, Y. Yamaguchi, C. Tull, "Intravascular probe for detection of vulnerable plaque," Proceedings of SPIE, Vol. 4508, 88-98, 2001, by fusing a regular optical fibers 45 with a scintillating fiber tip 47. The regular optical fiber 45 will be used for light delivery and the scintillating fiber tip 47 of several millimeters in length will be used for beta particle detection at the catheter tip. As those skilled in the art will certainly appreciate, there is a trade off between the length of the scintillating fiber tip 47 and the sensitivity of the positron detection. As such, those skilled in the art will appreciate that the length of the fibers may be varied without departing from the spirit of the present invention.

With regard to the scintillating fibers 46, the scintillating fibers 46 are very similar to conventional optical fibers except that they are doped with scintillating phosphors (1 ~2%) in the core. In accordance with a preferred embodiment, standard plastic scintillating fiber 46 from Bicron (Model # BCF-12) of 0.5 mm in outer diameter and 1.5 m in length are used. These fibers 46 have been used in testing to evaluate the sensitivity of the fiber and signal-to-noise ratio of the nuclear imaging data acquisition system. We have used sealed Ti-24 beta sources for the reported studies and the Ti-24 beta (765 keV β^-) source has very similar spectrum as ^{18}F (635 keV β^+). B. E. Patt, J. S. Iwanczyk, L. MacDonald, Y. Yamaguchi, C. Tull, "Intravascular Probe For Detection Of Vulnerable Plaque," Proceedings of SPIE, Vol. 4508, 88-98, 2001. Beta rays have a mean free path length of approximately 3mm before they interact with low-Z plastic scintillation detectors. The high-energy beta particles >600 keV trapped by the scintillating fibers 46 result in thousands of photons in the visible region (peak at 440nm), which produce a short light pulse. The plastic scintillator exhibits very fast luminescent-decay time (~3ns) and requires interface with a fast high-gain photomultiplier tube (PMT) 78 that is capable of resolving the first photoelectrons of a light pulse produced by the scintillator.

Since the detection sensitivity of the scintillating highly depends on the distance of the source to the scintillating fiber tip 47 and the number of scintillating fibers 46 used, we have evaluated the sensitivity of the present system by translating the source with a linear stage away from the scintillating fiber tips 47. The scintillating fibers 46 were grouped as 1, 2, 4, 6, respectively. Figure 6 shows that the sensitivity increases as the number of scintillating fibers 46 is increased and the sensitivity decreases as the fiber tip 47 to source distance is reduced.

Another parameter trade-off related to the hybrid catheter design is the sensitivity vs. resolution. To provide a higher spatial resolution for radiation detection, the scintillating fiber 46 length exposed to the radiation should be small. However, smaller scintillating fiber length will reduce the detection sensitivity. We have evaluated this trade-off by exposing the scintillating fiber tip 47 of 2 mm, 4mm, and 6 mm to the 1 uCi beta source and recording the total counts when the source was translated laterally. Six scintillating fibers were used for this test. Figure 7 shows the testing results which suggest that exposing fiber tip 47 of 6 mm to the radiation will reduce resolution by half but double the sensitivity.

To provide a higher spatial resolution for radiation detection, the scintillating fibers 46 at the proximal end to the catheter 12 tip region must be shielded from radiation, for example, with a sheath 49. In our prototype (described below) with a single scintillating fiber 46, a 6 mm scintillating fiber tip 47 was exposed to the beta source and the rest of the fiber was shielded with glass tubing 80.

In accordance with a preferred embodiment of the present invention, a 2x2 multianode photon multiplier tubes (PMT) 78 (R5900U-00-M4, Hamamatsu) is employed for detecting optical signals from the four scintillating optical fibers 46. This PMT 78 is very compact, about 30 mm by 30 mm by 24 mm in three dimensions and only 26 grams in weight. Its spectral response ranges from 300 to 650 nm with a peak at 420 nm, which is appropriate for this application. It features high-speed response and low cross talk. The typical value for anode pulse rise time is 1.2 ns, and the full width at half maximum of transit time spread is only 0.32 ns. The cross talk between different channels is generally less than 4%. The internal gain of R5900 is typically $5X10^5$, while the anode dark current per channel is about 0.5 nA (after 30 minutes storage in darkness).

Position sensitive PMT 78 is read out by a resistor divider chain producing +X, -X, +Y and -Y positions signals. Each of the signals will need to be preamplified, shaped with a linear amplifier and then converted from analog to digital. We will use four electronic channels connected to X_A, X_B, Y_C, Y_D outputs from the position sensitive PMT 78 (see Figure 8) to record the spectrum of each signal and the outputs will be weighted based on $(X\ Y) = (X_A/(X_A+X_B), Y_A/(Y_A+Y_B))$ to produce an approximate spatial map of the detected radiation activity. The spatial map will be displayed as hot spots. B. E. Patt, J. S. Iwanczyk, L. MacDonald, Y. Yamaguchi, C. Tull, "Intravascular Probe For Detection Of Vulnerable Plaque," Proceedings of SPIE, Vol. 4508, 88-98, 2001.

Attention is directed to possible optical cross-talk between scintillating fibers 46. Bicron scintillating fibers 46 are sealed well with the extramural absorber to minimize optical cross-talk. Residual cross-talk is measured by selectively transmitting light to each fiber 46 and measuring the outputs from the rest. If further sealing is needed, absorbing chambers will be added between scintillating fibers 46. The optical cross-talk between OCT fiber 26 and scintillating fiber 46 is readily removed by optical filter because the wavelength of the superluminescent diode source 54 of OCT is 1.3 μm, which is well above the emission peak (435 nm) of scintillating fibers 46.

As briefly discussed above, a control assembly 22 combines the OCT system 16 and a nuclear imaging based scintigraphy system 20 to creating a highly functional imaging system. In particular, the control assembly 22 includes 1) synchronization of OCT system and nuclear imaging system on data acquisition, 2) co-registration of OCT and nuclear imaging display, 3) use of a high-resolution OCT image to guide the high sensitivity nuclear imaging at suspicious vessel sections seen by OCT or use of high sensitivity nuclear imaging to guide the high-resolution OCT at suspicious vessel sections detected by nuclear imaging.

To demonstrate the feasibility of a combined OCT and radiation detection with co-registered position information, a prototype imaging device 10 was constructed and is shown in Figures 9 and 10. In this prototype, a GRIN lens 32 of 2.5mm outside diameter is placed inside a 3mm×3mm square glass tubing 80, and a 0.5mm scintillating fiber 46 is attached to the GRIN lens and positioned in one corner of the square tubing 80. The light from GRIN lens 32 is reflected 90°

by a tiny mirror, or prism, 34 attached to a rotation stage 81 through a shaft 82. The shaft 82 is also placed inside another piece of 3mm×3mm square glass tubing 84. The two glass tubings 80, 84 holding the GRIN lens 32 and the 90° reflection mirror 34 are aligned and separated about 10mm, in which space the 6 mm scintillating fiber 46 tip is exposed to air to avoid attenuation of beta radiation by the glass tubing 80, 84. The rotation stage 81 is driven by a DC motor 86 through a timing belt-pulley assembly, and the speed of the stage rotation can be controlled. It should be appreciated the motor 86 and the assembly are too big for an intravascular catheter and the embodiments described above disclosed designs for the implementation of the present imaging device for *in vivo* usage. Since OCT A-line scanning speed is configured to be 64Hz, 512 A-lines are obtained in one revolution of the 90° reflection mirror, and the OCT signal is processed to have circumferential display corresponding to the cross-section of the blood vessel.

To demonstrate the simultaneous OCT structural imaging and radiation detection, we have acquired co-registered OCT and radiation data from freshly excised pieces of bovine coronary arteries. For the convenient of experiments, the examined artery is translated in 2mm steps, and an OCT across-section image and radiation counts are acquired simultaneously at each step. The beta source is positioned closer to a hole left at the artery and translated with the artery. Figures 11 and 12 show the co-registration result. When the beta source reaches the scintillating fiber 46 detection range, the total photon counting is increased significantly. When the beta source is away from the detection range of the fiber 46, the total photon counting reduces to background level. The spatial resolution of the radiation detection is poor because a 6 mm single scintillating fiber tip 47 was exposed to the beta source. The resolution can be improved by exposing smaller fiber tip 47 to the source as discussed before. Nevertheless, the feasibility of co-registration can be readily demonstrated from this result.

We plan to study light attenuation issues using the recirculation perfusion system shown in Figure 13. The perfusion loop consists of a peristaltic pump 88, a 1×2 flow switch 90, a damper 92, a perfusion guide 94 through the blood vessel 96 and biocompatible plastic tubing 98. When the perfusion is through the damper 92, a continuous flow will be applied; when the perfusion is

bypassing the damper 92, a pulsatile flow will be generated by the peristaltic pump 88. The perfusion rate is controlled by changing the speed of pump. This perfusion system allows for the infusion of buffer (phosphate buffer saline) in the absence and presence of simulated pulsatile flow, with or without porcine red blood cells. Based on our experience in OCT blood flow studies, diluted blood to a quarter of its concentration will not cause significant light attenuation for the vessel size of less than 1 millimeter in diameter. We will further test our catheter-based OCT system with different concentrations of red blood cells. The OCT catheter will be advanced and images will be taken within an intact pig vascular segment (2 cm in length), which is interfaced with the recirculating system. The buffer with different amounts of red blood cells will be perfused within the recirculation system. The OCT image quality will be analyzed and results obtained will answer questions for future *in vivo* studies in larger animal models regarding how often and how much saline is needed for the flushing. The agents that have been reported to enhance the light penetration to 120-150% include glucose, dextrans, propylene glycol and trazograph. V. Tuchin, X. Xu, and R. K. Wang, "Dynamic Optical Coherence Tomography In Studies Of Optical Clearing, Sedimentation, And Aggregation Of Immersed Blood," Applied Optics, Vol 41(1): 258:271, 2002. We will study glucose and dextrans in conjunction with saline flush in an attempt to find whether saline flush can be avoided or not. If saline flush is required, we will find the optimal amount of saline water in the presence of each of the agents.

For sensitive detection of beta activities, the background gamma radiation needs to be estimated and subtracted. For *in vivo* beta imaging, circulating blood will contain certain amount of beta and gamma activities and the total count rate will be the summation of both activities, which will contaminate the actual count rates measured at the lesion locations. We will use the recirculation system shown in Figure 13 to assess the background gamma activities in the absence and presence of circulating blood that carries certain amount of radioactive agents. To evaluate spatial resolution within the arterial wall various amounts of ^{18}F (from 1 nCi to 1 uCi) in 10 microliters of solvent will be injected into the arterial wall. The exact amount injected into the vessel wall will be calculated by measuring the activity left in the syringe. The catheter will be advanced back and forth and detected counts will be registered. The profile of the activity versus location will

be plotted, and the full width at half maximum of the activity profile will be determined. Similar analyses will be performed for different scintillating fiber thickness and numbers in the catheter for different amounts of radioactivity. In addition to localization along the artery, we will evaluate the circumferential spatial resolution for multifiber catheter designs. The trade-off between the spatial resolution (related to the length of the scintillating fiber tip) and the sensitivity of radiation detection will be evaluated. In addition, the data acquisition time needed to obtain total counts with high activity vs background ratio will be evaluated. The same piece of artery may be used for several evaluations depending on the spatial resolution. To evaluate the system in the presence of higher levels of background activity these experiments will be repeated in the absence and presence of different amount of circulating ^{18}F and background radiation will be estimated for each level of activity. We will also take advantage of the relative short half-life of ^{18}F to evaluate the count sensitivity of the system.

Induction of experimental atherosclerosis in rabbits will be employed in testing the efficacy of the present imaging device as further development proceeds. Specifically, New Zealand White (NZW) rabbits (4-5 mon old) weighing 2.5 to 3.0 kg will be fed a 0.5% cholesterol diet custom mixed in 6% peanut oil; the non-injured control animals will be fed normal rabbit chow. One week following initiation of the high-fat diet, anesthetized rabbits will undergo deendothelialization of the infra-diaphragmatic aorta with a 4F Fogarty embolectomy catheter passed via right femoral artery. Rabbits will be continued on the hyperlipidemic diet for 4 months. NZW rabbit is large enough to allow in vivo testing of the proposed hybrid intravascular OCT/scintillator catheter.

Rabbits will be injected intravenously with ^{18}Fdeoxyglucose (FDG), and the hybrid intravascular OCT/scintillator catheter will be placed in the aorta for imaging under fluoroscopic guidance. We anticipate optimal uptake in the aorta approximately 30 mins after radiotracer injection. Serial blood samples will be drawn for evaluation of blood clearance of the radiotracer. Rabbits will be euthanized after in vivo imaging. The injured segment of the aorta will then be placed on our perfusion apparatus for ex vivo imaging. Following ex vivo imaging, the entire length of the aorta will be exposed and cleaned of adherent adventitial fat and connective tissue and removed for ex vivo analysis. The entire aorta will then be segmented into 2 mm pieces. These

segments will be weighed and counted in an automatic well-type gamma counter for determination of the percent injected dose per gram tissue (%ID/g) of the radiolabeled ligands. The aortic specimens will then be submitted for histopathological studies.

Pathological characterization of the aortic atherosclerotic lesions will be undertaken by histological assessment and immunohistochemical evaluation of the constituents of neointimal layer. Histochemical staining will also be performed for determining the distribution of macrophages, and the presence of apoptosis of macrophages. Prevalence of macrophages will be correlated between %ID/gram uptake of ^{18}Fdeoxyglucose.

We will evaluate the hybrid OCT/scintigraphy device for *ex vivo* analysis of vascular structure and function in normal (n = 6) and atherosclerotic (n = 6) NZW rabbit aorta, comparing imaging results with postmortem histology and tissue counting. In the final phase of testing, we will establish the feasibility of *in vivo* imaging with the Hybrid OCT/ scintigraphy intravascular catheter in normal (n = 6) and abnormal atherosclerotic rabbit aorta (n = 6). As previously outlined, NZW rabbits on hyperlipidemic diet with endothelial injury will be utilized for a subset of the *ex vivo* and *in vivo* studies. The *in vivo* images will be directly compared with images acquired from the same rabbit aortas mounted on our *ex vivo* testing system. This initial testing will establish resolution of the OCT system under true conditions of pulsatile flow in the presence of circulating blood. We anticipate that the catheter system will require incorporating a flushing system immediately proximal to the active imaging component of the catheter. In the rabbit model, the flushing will be initially accomplished with a long sheath placed in the aorta via the carotid with the aid of a guide wire. After the guide catheter is positioned, the guide wire will be withdrawn, and the hybrid catheter will be advanced through the guide catheter with the imaging component just distal to the guide catheter. The OCT images and the radiation counts will be acquired while flushing between the OCT catheter and blood vessel is periodically conducted. However, a flushing system ultimately will need to be integrated with the catheter.

A total of 24 rabbits will be utilized over a two year period, recognizing approximately a 25% loss rate. Initial testing of the hybrid OCT/ scintigraphy catheter will be performed on porcine coronary vascular tissue, however, subsequent *ex vivo* testing will be performed on NZW rabbits.

Final testing of intravascular anatomic and functional FDG imaging will be conducted in atherosclerotic NZW rabbits as outlined above.

While the preferred embodiments have been shown and described, it will be understood that there is no intent to limit the invention by such disclosure, but rather, is intended to cover all modifications and alternate constructions falling within the spirit and scope of the invention as defined in the appended claims.

CLAIMS

1. An imaging device, comprising:

a delivery device shaped and dimensioned for accessing a predetermined body cavity or lumen;

an OCT system linked to the delivery device; and

a nuclear imaging system linked to the delivery device.

2. The imaging device according to claim 1, further including a control assembly linked to the OCT system and the nuclear imaging system, the control assembly includes processing means adapted for gathering information from the OCT system and the nuclear imaging system and creating imaging information used in the assessment of the body cavity or lumen into which the delivery device is placed.

3. The imaging device according to claim 1, wherein the OCT system includes scanning components housed within the delivery device and an OCT source assembly remote from the delivery device.

4. The imaging device according to claim 3, wherein the scanning components of the OCT system include an optical fiber extending from the OCT source assembly through the length of the catheter, a lens secured to a distal end of the optical fiber and a rotating right angle prism positioned for receiving light from the lens.

5. The imaging device according to claim 4, wherein rotation of the right angle prism is controlled by a motor coupled to the right angle prism.

6. The imaging device according to claim 5, wherein the motor is housed within a distal end of the delivery device.

7. The imaging device according to claim 5, wherein the motor is positioned adjacent a proximal end of the delivery device.

8. The imaging device according to claim 1, wherein the nuclear imaging system includes scintillating fibers positioned adjacent a distal end of the delivery device.

9. The imaging device according to claim 8, wherein the scintillating fibers are sheathed in the area adjacent a proximal end of the delivery device.

10. The imaging device according to claim 8, wherein two to six scintillating fibers are positioned adjacent the distal end of the delivery device and are adapted for determining the radial position of a radiation source.

11. The imaging device according to claim 8, wherein the scintillating fibers are coupled to a proximal end of the delivery device by optical fibers extending from the scintillating fibers to the proximal end of the delivery device.

12. A method for imaging body lumens or cavities, comprising the following steps:

inserting a delivery device to a predetermined location within a body previously marked with radioactive markers, the delivery device including an OCT system linked to the delivery device and a nuclear imaging system linked to the delivery device;

scanning the predetermined location with the OCT system for obtaining a high resolution image and sensing the radioactive markers with the nuclear imaging system to obtain a high contrast image of the predetermined location.

13. The method according to claim 12, further including the step of processing information from the OCT system and the nuclear imaging system and creating imaging information used in the assessment of the body cavity or lumen into which the delivery device is placed.

14. The method according to claim 12, wherein the predetermined location is vessels of the cardiac system.

15. The method according to claim 12, wherein the predetermined location is chosen from the group consisting of the cardiac system, the gastrointestinal system and the pulmonary system.

16. The method according to claim 12, wherein the nuclear imaging system includes at least one scintillating fiber positioned adjacent a distal end of the delivery device.

17. The method according to claim 16, wherein the scintillating fiber is sheathed in the area adjacent a proximal end of the delivery device.

18. The method according to claim 16, wherein two to six scintillating fibers are positioned adjacent the distal end of the delivery device and are adapted for determining the radial position of a radiation source.

19. The method according to claim 16, wherein the scintillating fiber is coupled to a proximal end of the delivery device by an optical fiber extending from the scintillating fiber to the proximal end of the delivery device.

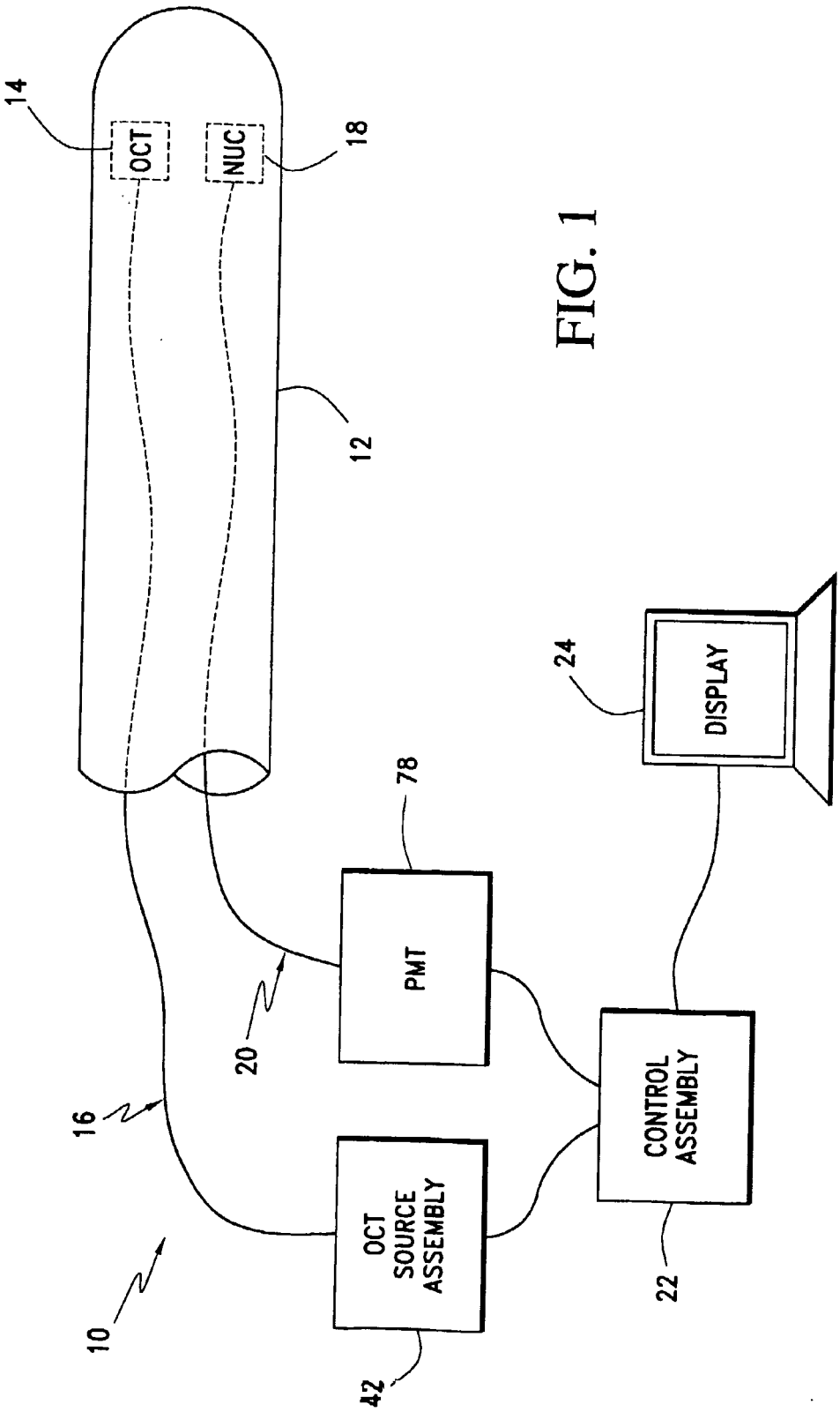
14
OCT
NUC
18
12
24
DISPLAY
78
PMT
20
16
CONTROL ASSEMBLY
OCT SOURCE ASSEMBLY
10
22
42

FIG. 1

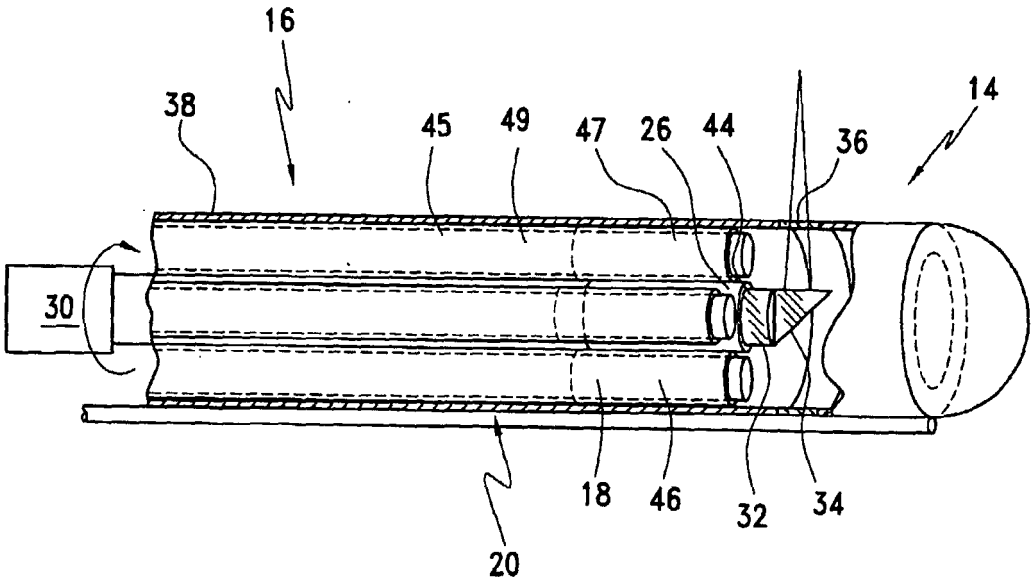
16
38
45
49
47
26
44
36
14
30
18
46
32
34
20

FIG. 2

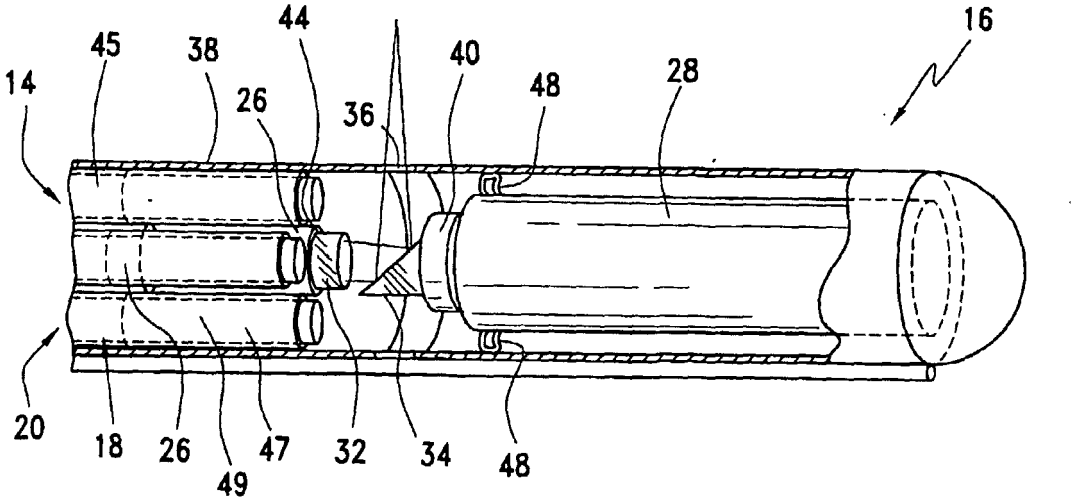
44
16
45
38
40
14
26
36
48
28
20
18
26
49
47
32
34
48

FIG. 3

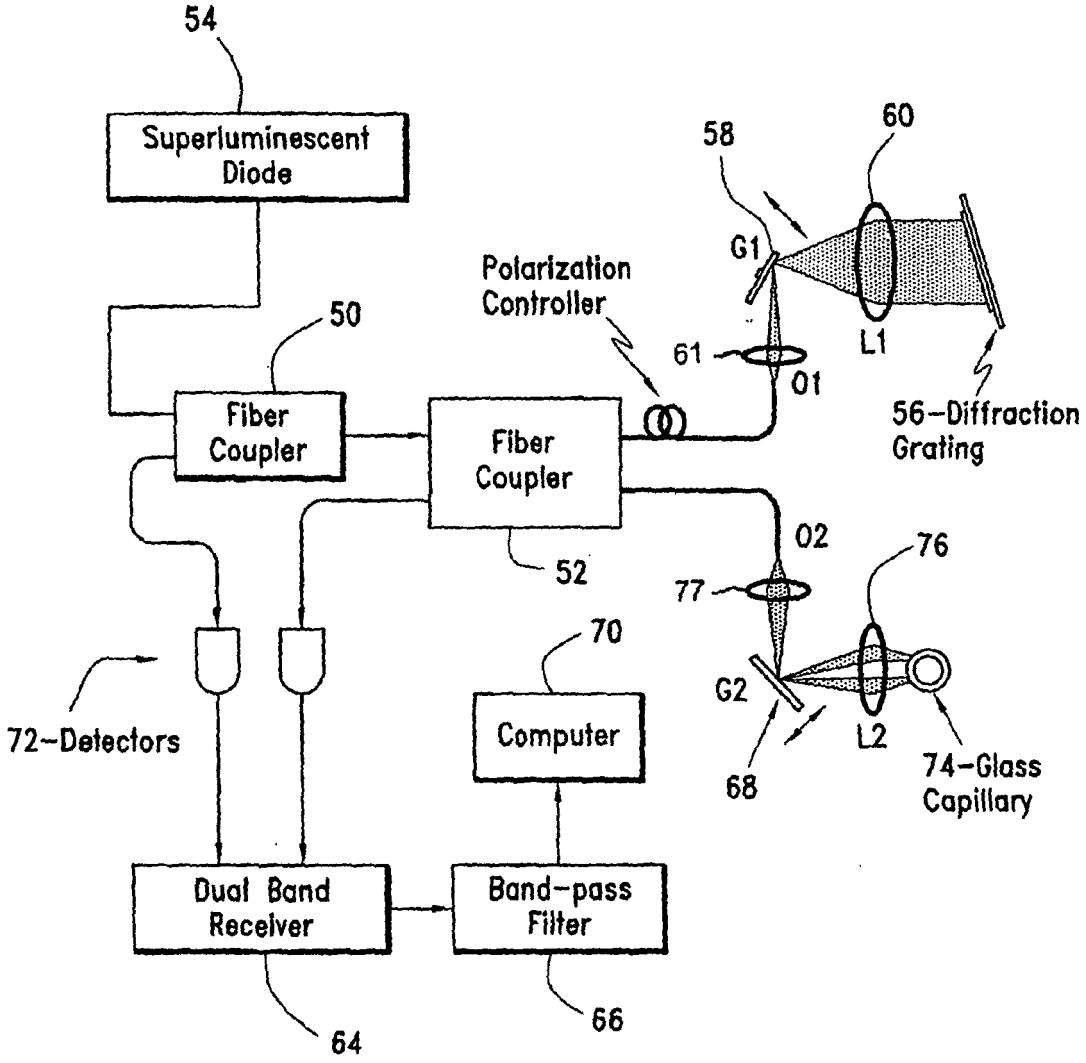
54
Superluminescent Diode
50
Fiber Coupler
Polarization Controller
Fiber Coupler
52
58
60
G1
61
01
L1
56-Diffraction Grating
02
77
76
G2
68
L2
74-Glass Capillary
70
Computer
72-Detectors
Dual Band Receiver
Band-pass Filter
64
66

FIG. 4

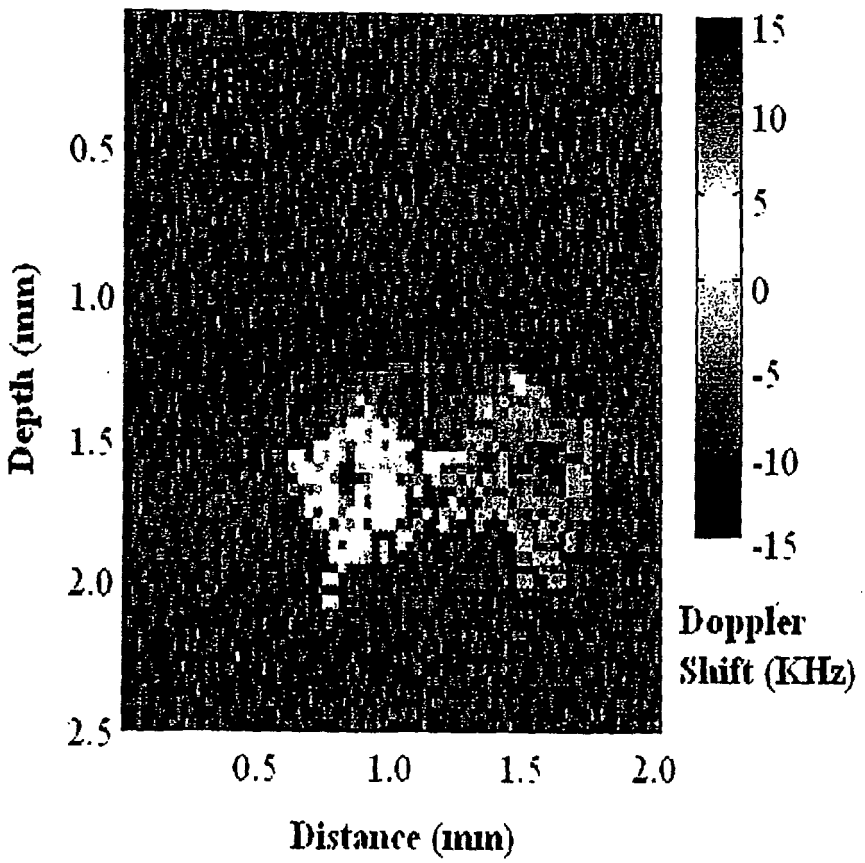
Depth (mm)
0.5
1.0
1.5
2.0
2.5
0.5
1.0
1.5
2.0
Distance (mm)
15
10
5
0
-5
-10
-15
Doppler
Shift (KHz)

FIG. 5

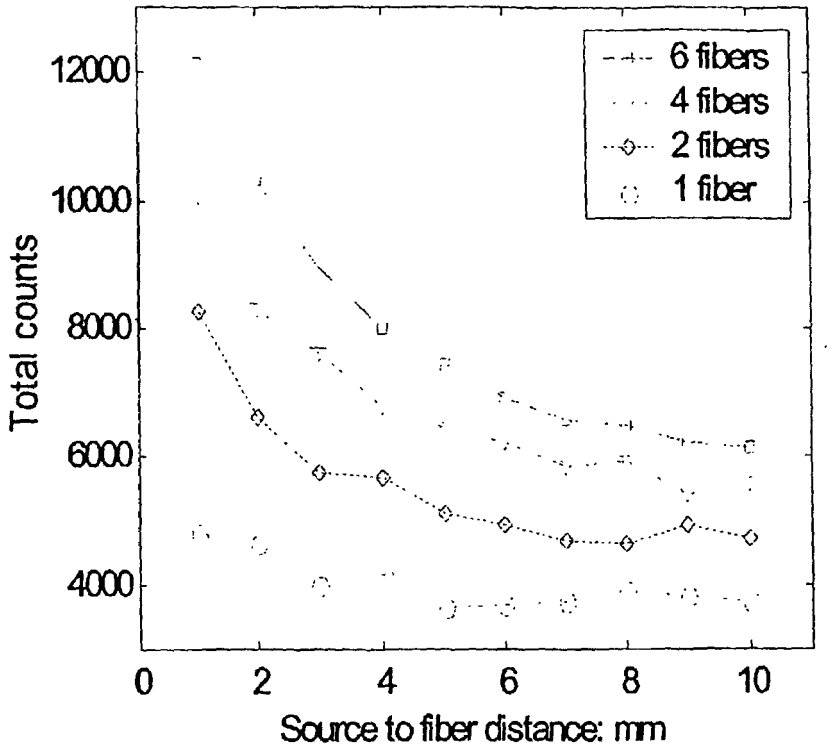
6 fibers
4 fibers
2 fibers
1 fiber
Total counts
12000
10000
8000
6000
4000
0
2
4
6
8
10
Source to fiber distance: mm

FIG. 6

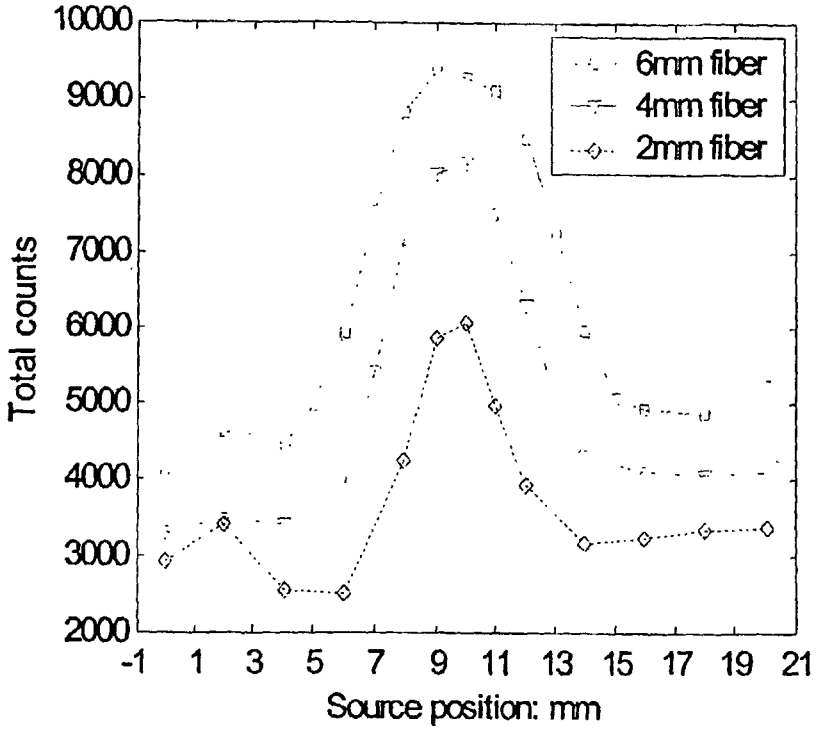
10000
9000
8000
7000
6000
5000
4000
3000
2000
Total counts
-1
1
3
5
7
9
11
13
15
17
19
21
Source position: mm
6mm fiber
4mm fiber
2mm fiber

FIG. 7

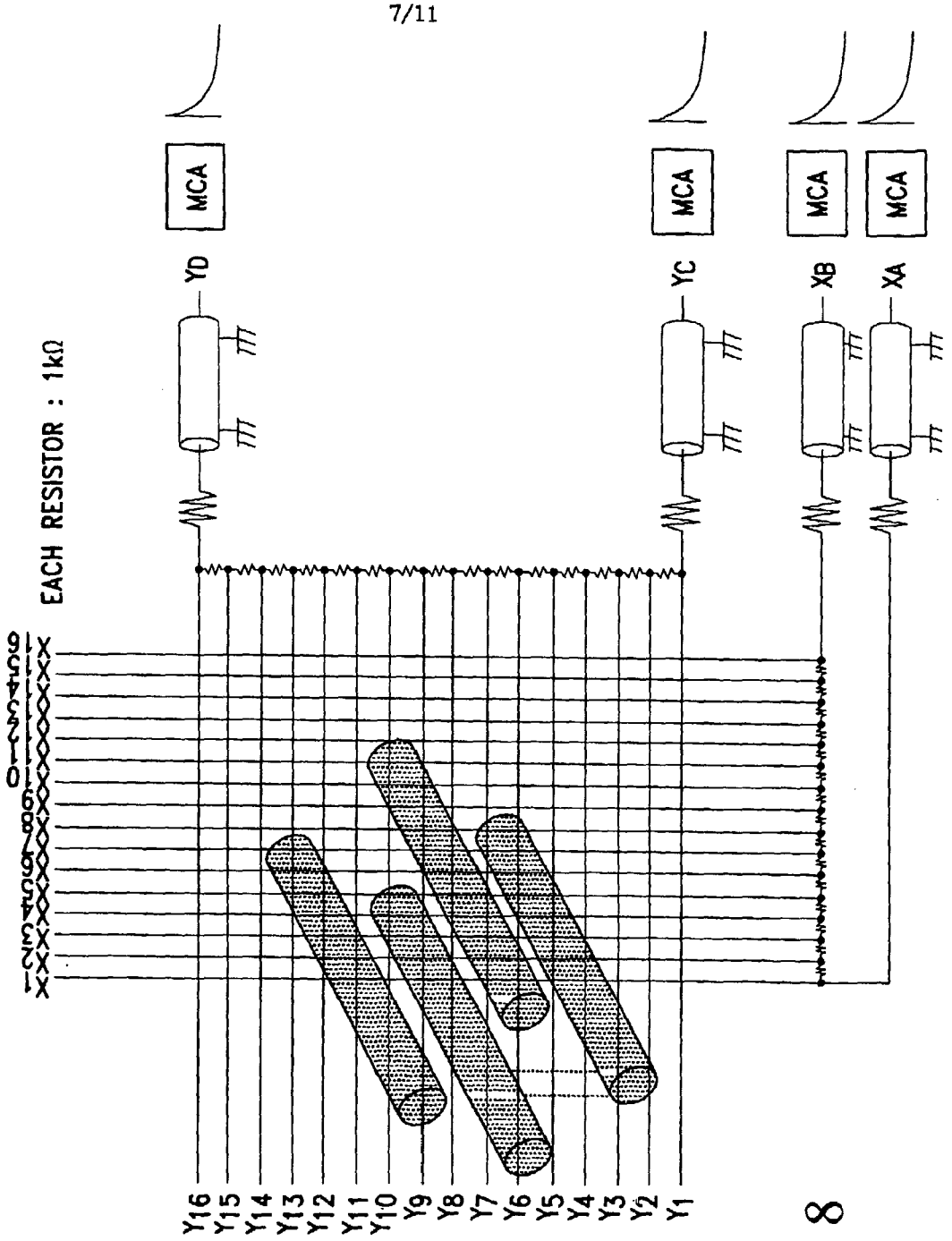
MCA
MCA
MCA
MCA
YD
YC
XB
XA
EACH RESISTOR : 1kΩ
X16
X15
X14
X13
X12
X11
X10
X9
X8
X7
X6
X5
X4
X3
X2
X1
Y16
Y15
Y14
Y13
Y12
Y11
Y10
Y9
Y8
Y7
Y6
Y5
Y4
Y3
Y2
Y1

FIG. 8

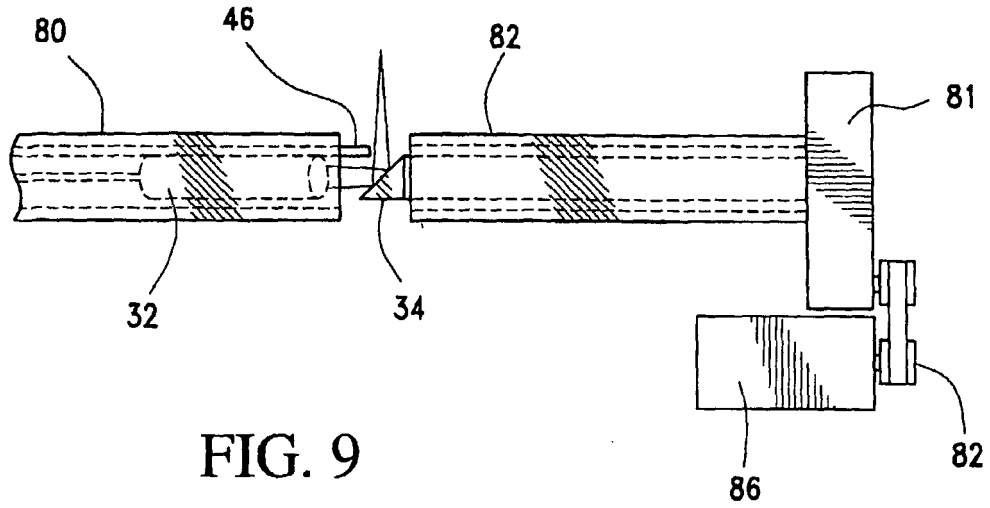

FIG. 9

FIG. 10

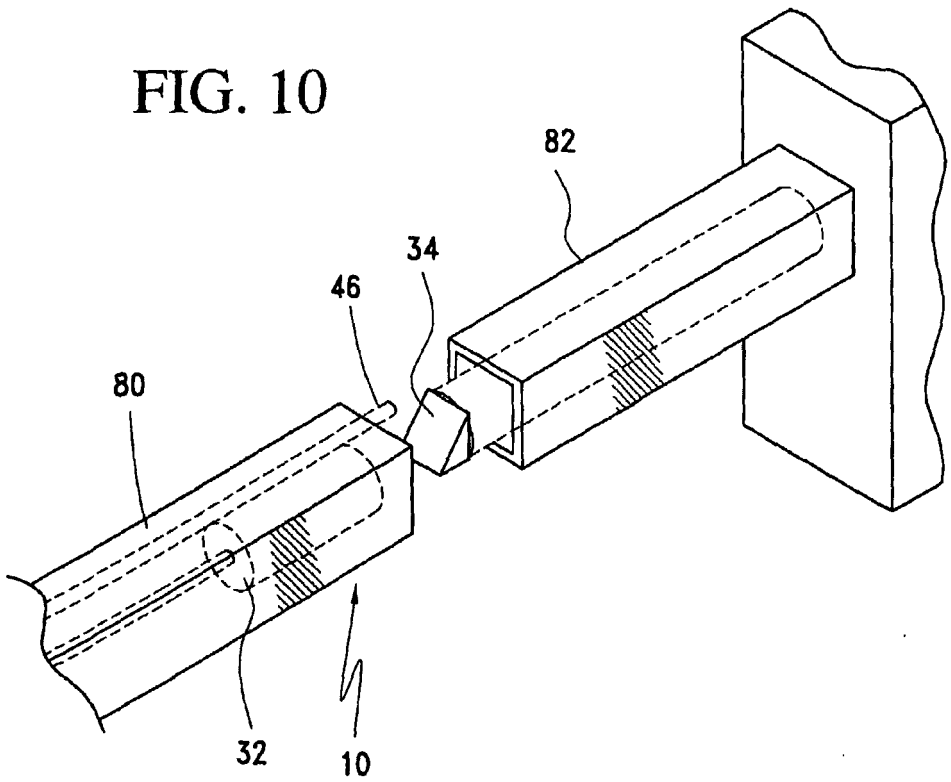

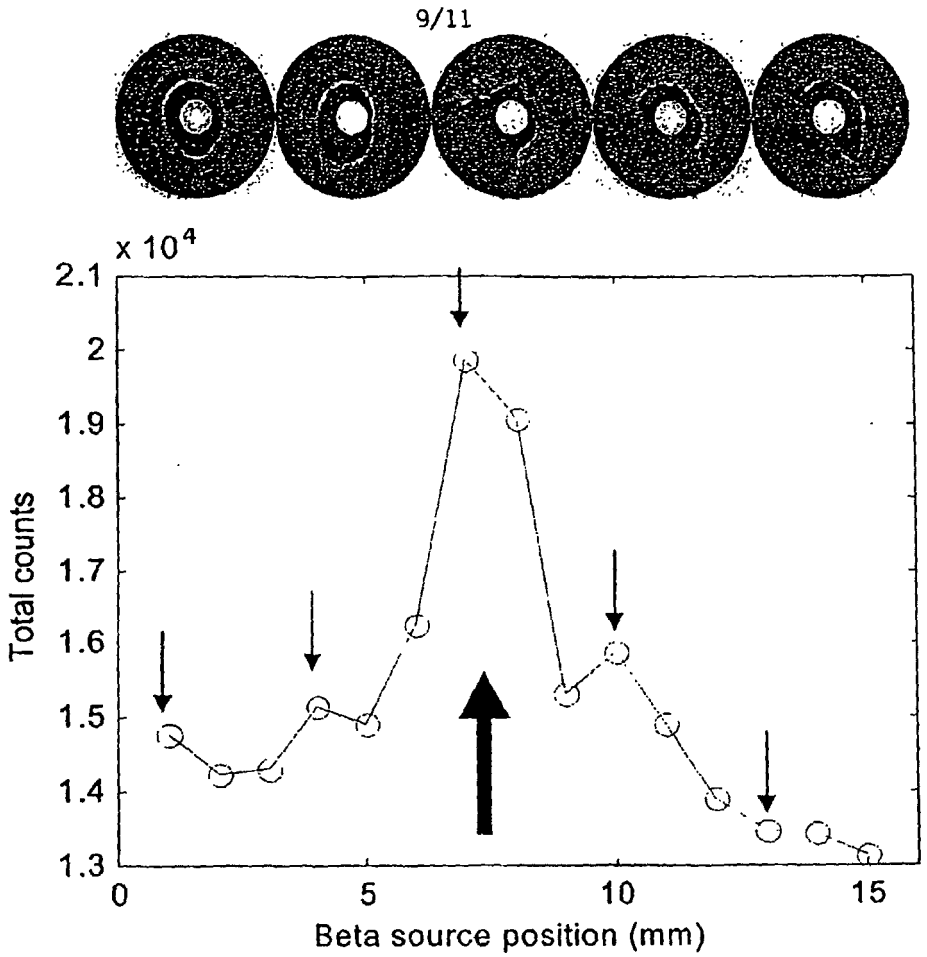
x 10^4
2.1
2
1.9
1.8
1.7
1.6
1.5
1.4
1.3
Total counts
0
5
10
15
Beta source position (mm)

FIG. 11

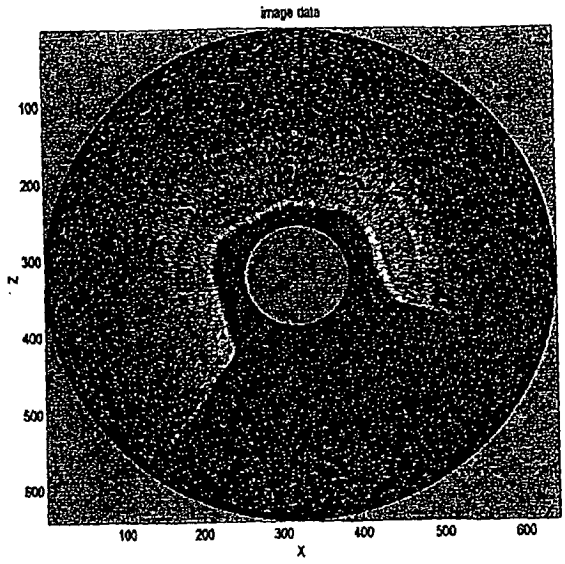

FIG. 12

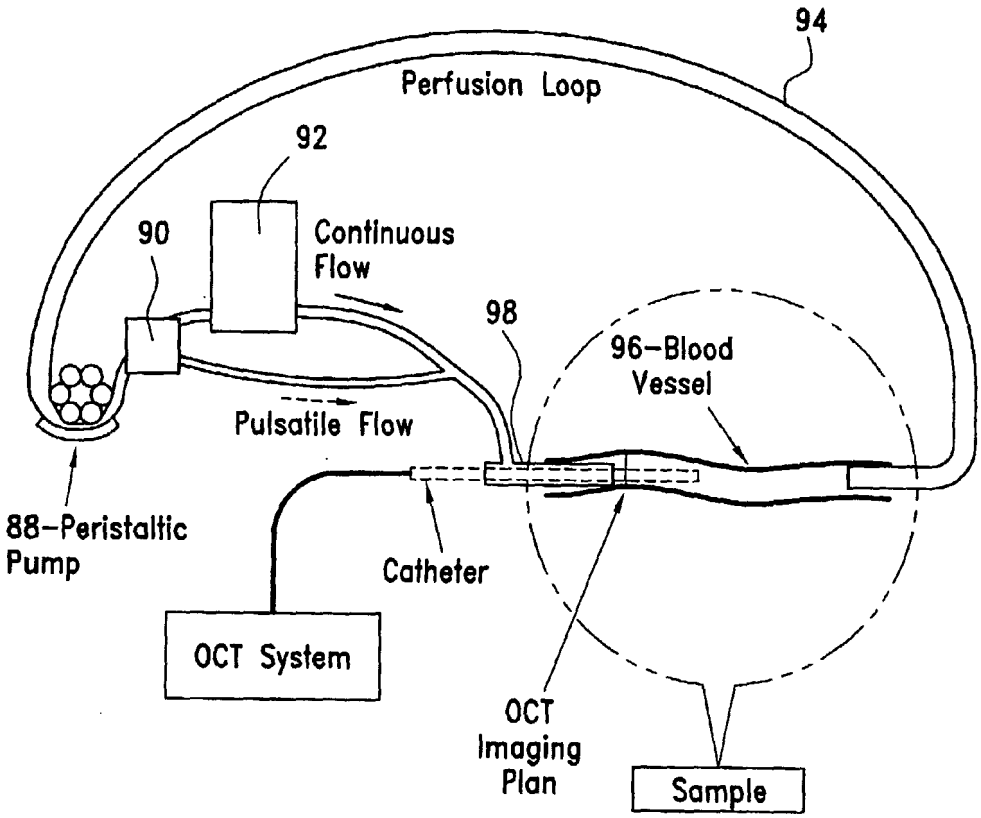
94
Perfusion Loop
92
90
Continuous
Flow
98
96-Blood
Vessel
Pulsatile Flow
88-Peristaltic
Pump
Catheter
OCT System
OCT
Imaging
Plan
Sample

FIG. 13

APPENDIX

SINU-001-PCT

IN THE UNITED STATES PATENT AND TRADEMARK OFFICE
APPLICATION FOR LETTERS PATENT

INVENTORS:
Albert J. Sinusas
Quing Zhu
Mehran M. Sadeghi

TITLE:
HYBRID OCT/SCINTIGRAPHY INTRAVASCULAR DEVICE

1120 OPTICS LETTERS / Vol. 28, No. 13 / July 1, 2003

Doppler angle and flow velocity mapping by combined Doppler shift and Doppler bandwidth measurements in optical Doppler tomography

Daqing Piao

Department of Electrical and Computer Engineering, University of Connecticut, Storrs, Connecticut 06269-2157

Linda L. Otis

School of Dental Medicine, University of Pennsylvania, Philadelphia, Pennsylvania 19104-6003

Quing Zhu

Department of Electrical and Computer Engineering, University of Connecticut, Storrs, Connecticut 06269-2157

Received October 25, 2002

Accurate estimation of flow velocity requires measurement of Doppler angle, which is not available in general clinical applications. We describe a novel method of direct Doppler angle and flow velocity mapping that uses a conventional single-beam optical Doppler tomography system. The Doppler angle is estimated by combination of Doppler shift and Doppler bandwidth measurements, and flow velocity is calculated from the Doppler shift and the estimated Doppler angle. *In vivo* study of lip microvascularization demonstrates that this method is capable of providing both flow speed and flow direction information. © 2003 Optical Society of America

OCIS codes: 170.4500, 170.3880.

Optical Doppler tomography (ODT),[1-3] a functional extension of optical coherence tomography,[4] has found wide clinical applications in detection and estimation of subsurface blood flow velocity. Compared with ultrasonic Doppler flow mapping and laser Doppler velocimetry, ODT has advantages of high spatial resolution and high volumetric flow sensitivity. In ODT, the Doppler frequency shift of an interference signal between the light backscattered from the moving scatterers and light reflected from the reference mirror is detected and is proportional to the mean flow velocity of moving scatterers. For a scatterer that is moving perpendicularly to the probe beam, the Doppler shift vanishes; for a scatterer that is moving obliquely to the probe beam, however, flow velocity cannot be accurately estimated from the Doppler shift without knowledge of the Doppler angle. Doppler angle measurement with a double-beam technique in which two probe beams were oriented at a precisely known relative angle was originally invented for Doppler ultrasound[5] and has also been extended to ODT.[6] The double-beam technique in ODT, however, requires two optical beams with different polarizations for probing the target; in addition, the beams demand multichannel detection electronics and polarization-maintaining fiber optics. Moreover, the double-beam setup at the sample arm is apparently inconvenient for *in vivo* application. Doppler bandwidth is known in ultrasound and laser Doppler velocimetry to be the effect of transit time broadening in which the output signal bandwidth is altered by moving scatterers that cross the probing beam.[7] In ODT, Ren *et al.* reported detection of a velocity component that is transverse to the optical probing beam with the Doppler bandwidth measurement.[8] As was reported, Doppler bandwidth is insensitive to the variation of Doppler angle when the angle is within $\pm 15°$ perpendicular to the probe beam. However, inasmuch as *a priori* knowledge of Doppler angle is unavailable, the Doppler bandwidth only is not sufficient for accurate estimation of the flow velocity. In addition, Doppler bandwidth does not provide directional information on the flow. Doppler angle measurement thus ultimately limits the accuracy of flow velocity estimation. In this Letter we present what is to our knowledge a novel method of Doppler angle and flow velocity estimation by use of a conventional single-beam ODT system. The Doppler angle is estimated by combination of Doppler shift and Doppler bandwidth measurements, and flow velocity is calculated by use of Doppler shift and the estimated Doppler angle. The estimation accuracies of Doppler angle and flow velocity were previously evaluated in Intralipid flow experiments with predefined Doppler angle and flow velocity values.[9] We found in the study reported in Ref. 9 that the accuracies of Doppler angle and flow velocity are greater than 95% and 90%, respectively, for an average signal-to-noise ratio (SNR) 13 dB from Intralipid. The *in vivo* imaging capability of recovering both flow direction and flow speed by this method is demonstrated in this Letter with human lip microvascularization.

In ODT, after Doppler shift $\bar{f}$ and full width at half-maximum Doppler bandwidth Δf are measured, the Doppler angle θ can be obtained:

$$\theta = \tan^{-1}\left(\frac{4}{\pi\sqrt{\ln 2}}\frac{1}{\mathrm{NA}_{\mathrm{eff}}}\frac{\Delta f - b}{\bar{f}}\right), \tag{1}$$

where $\mathrm{NA}_{\mathrm{eff}}$ is the effective numerical aperture of the probe light inside the sample and b accounts for a system-specified spectrum bandwidth background that is independent of the macroscopic flow velocity.[8] The flow velocity is then calculated with

$$v = \frac{\bar{f}\lambda}{2\cos\theta}. \tag{2}$$

0146-9592/03/131120-03$15.00/0

Equations (1) and (2) are not valid when the Doppler shift is zero, in which case the Doppler angle is considered to be 90° and the flow velocity is calculated from the Doppler bandwidth with

$$v = \frac{2}{\pi\sqrt{\ln 2}} \frac{\lambda}{\mathrm{NA}_{\mathrm{eff}}} (\Delta f - b). \quad (3)$$

The ODT system for *in vivo* study was described in detail in Ref. 10. In addition to obtaining the intensity profile, each cross-sectional data set is processed to yield Doppler shift and Doppler bandwidth images. The Doppler shift is calculated with a previously introduced sliding-window filtering technique,[10] and this technique is extended to Doppler bandwidth measurement.[9] The background spectrum bandwidth [b in Eq. (1)] is found to be 5.1 kHz, and the effective numerical aperture of the probe beam inside the tissue is equal to 0.08.

The *in vivo* blood flow was taken at the upper lip of a female volunteer. The probe beam from the graded-index lens was oriented close to 90° with respect to the surface of the imaging spot. The spot of ODT scan was taken at the pars villosa of the lip, which has the most extensive subsurface blood supply. It is reported that in the pars villosa of the lip, the papillary loop network is the most characteristic.[11] The pars villosa contains two types of loop: short loops and long loops (see Fig. 1). The short loops (~250 μm in length) are papillary networks in contact with the deep aspect of the epidermis. The long loops (~700 μm in length), which are more numerous, penetrate deep into the papillary layer of the dermis. The loops are arranged perpendicularly to the periphery of the lip. The papillary network connects with the reticular network. The reticular network is composed of two distinct parts: a superficial part and a deep part. The superficial part essentially receives the short loops and has the appearance of fine, irregular meshes arranged parallel to the surface. The deep part drains the superficial part of the reticular network and the long loops of the papillary network.

Figure 2(a) is the Doppler shift image superimposed on structure image, which reveals a flow region (spot 1). The apparent distortion of the structural image is due to the respiratory motion at a period of approximately 4.6 s. Nevertheless, this respiratory motion is found to be out of the range that could introduce artifacts into Doppler shift and Doppler bandwidth images. Figure 2(b) shows the Doppler bandwidth image. Compared with Fig. 2(a), there is one smaller flow region (spot 2) shown in addition to spot 1 in Fig. 2(b). Flow spot 2 has a Doppler angle very close to 90° and is not identifiable in Fig. 2(a). Spot 1 in Fig. 2(b) appears as one large flow region, however, in Fig. 2(a) it shows up as two regions with opposite flow directions. Figure 2(c) is the local Doppler angle mapping of spots 1 and 2 based on the values calculated with Eq. (1) and superimposed on the structure image for better visualization. The downtilted arrows inside the solid circle of spot 1 represent a Doppler angle greater than 90°, and the uptilted arrows inside the dashed circle represent a Doppler angle less than 90°. The horizontal arrows in spot 2 represent flow that is perpendicular to the probe beam. With local Doppler angle information, the calculated flow velocity vector image is shown in Fig. 2(d). Both spot 1 and spot 2 show up in velocity mapping, and the small negative flow region (blue color) in spot 1 is clearly identified. The flow areas in spots 1 and 2 are approximately 700 μm in depth and 600 μm in length and have a maximum flow velocity of ~100 mm/s. To our knowledge, there is no literature information regarding human lip blood flow speed; however, the blood vessel sizes that we measured agree well with those reported in anatomic studies.[11] Based on the location and size, we believe that the larger flow region in spot 1 and the flow area in spot 2 are all long loops. In the velocity image Fig. 2(d), there is a discrete strip of flow region that is parallel to the surface (depicted by the neighboring white strip), which is also shown in Fig. 2(c) with close-to-90° Doppler angle. Based on the depth and orientation, we believe that this is the superficial part of the reticular network.

It has been shown in this Letter that Doppler bandwidth imaging is more robust than Doppler shift imaging, particularly in detecting close-to-90° blood flows. This is not a surprise because for the Doppler angle in the region of 90° Doppler bandwidth is angle insensitive, whereas the Doppler shift is highly dependent on the angle. The angle insensitivity of the Doppler bandwidth, however, limits the sensitivity of flow velocity estimation if it is based solely on Doppler bandwidth. Furthermore, the Doppler bandwidth–only imaging does not provide flow direction information. The Doppler shift, on the other hand, is direction dependent. By combining Doppler shift and Doppler bandwidth measurements, one can form local Doppler angle and flow velocity vector mapping, which preserves the robustness of Doppler bandwidth detection while maintaining velocity sensitivity and

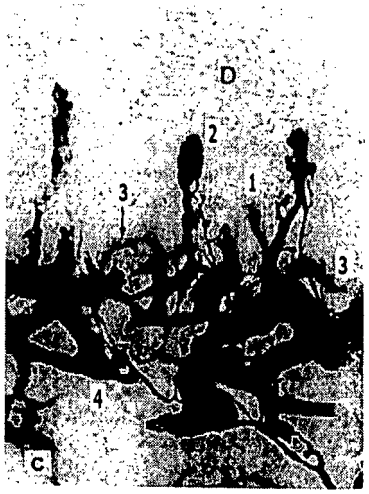

Fig. 1. Picture of microvascularization of the pars villosa, taken from Ref. 11 (reprinted with permission from S. Karger, AG, Basel), where 1 is a short loop, 2 is a long loop, 3 is the superficial part of the reticular network, and 4 is the deep part of the reticular network.

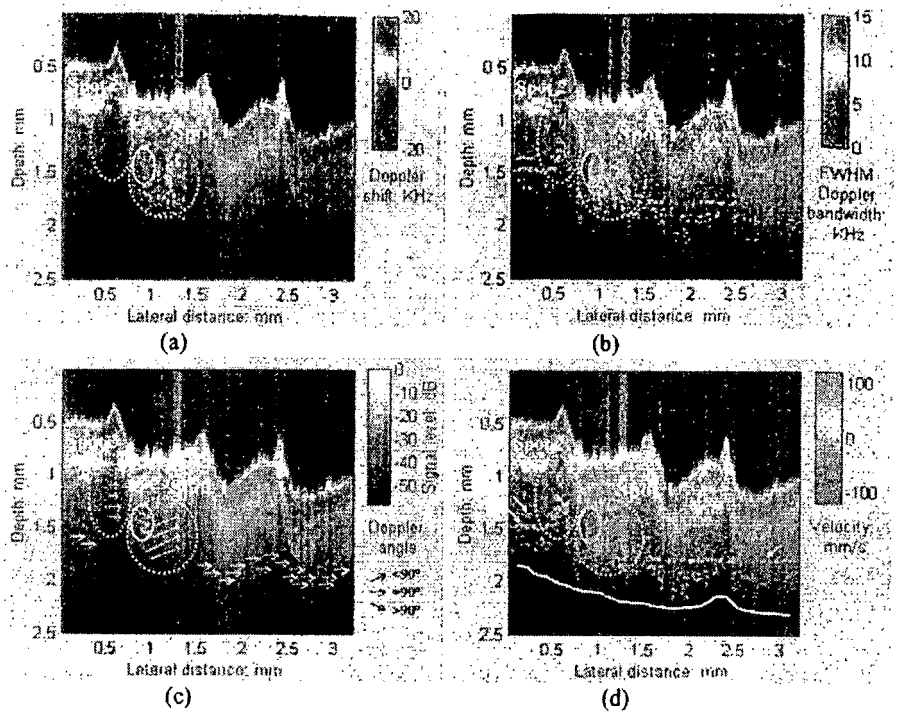

Fig. 2. (a) Doppler shift image superimposed on a structural image taken from the pars villosa of the upper lip of a female volunteer. In spot 1, the two regions of blood flow are in opposite directions. (b) Doppler bandwidth image superimposed on structural image. The smaller flow spot 2 is not detected in (a). (c) Doppler angle mapping depicted based on the calculated values with Eq. (1), where the three flow regions in spots 1 and 2 are represented with arrows of different orientations. (d) Velocity mapping calculated by Doppler shift and estimated Doppler angle. Three flow regions in spots 1 and 2 are clearly identified.

flow direction information of Doppler shift imaging. As was shown, this new ODT imaging method introduced is capable of identifying more blood vessels and blood volumes as well as the directions of flow. The average SNR of the flow areas imaged is found to be approximately 10 dB. Although this SNR of *in vivo* tissue is less than that of Intralipid in our previously mentioned experiments,[9] simulations have shown that at this SNR greater than 90% and 85% accuracies for Doppler angle and flow velocity estimations are expected, respectively. One deficiency of flow velocity mapping is the lack of color-coding discrimination between 90° flow and positive flows; however, this can be easily overcome by integration with Doppler angle mapping.

To conclude, we have presented a novel method of direct Doppler angle and flow velocity mapping by combining Doppler shift and Doppler bandwidth measurements in ODT. This method can be directly implemented to conventional single-beam ODT without hardware modification. The *in vivo* blood flow scanning in human lip demonstrates that lip microvascularization can be better identified with both flow speed and flow direction.

This work was partially supported by a research grant from the National Institutes of Health (NIH 1R01 DE11154-03). The authors acknowledge receiving a predoctoral training grant from the Department of Defense (DAMD17-02-1-0358). D. Piao and Q. Zhu's e-mail addresses are piao@engr.uconn.edu and zhu@engr.uconn.edu, respectively.

References

1. X. J. Wang, T. E. Milner, and J. S. Nelson, Opt. Lett. **20,** 1337 (1995).
2. Z. P. Chen, T. E. Milner, S. Srinivas, X. J. Wang, A. Malekafzali, M. J. C. Van Germert, and J. S. Nelson, Opt. Lett. **22,** 1119 (1997).
3. J. A. Izatt, M. D. Kulkarni, S. Yazdanfar, J. K. Barton, and A. J. Welch, Opt. Lett. **22,** 1439 (1997).
4. D. Huang, E. A. Swanson, C. P. Lin, J. S. Schuman, W. G. Stinson, W. Chang, M. R. Hee, T. Flotte, K. Gregory, C. A. Puliafito, and J. G. Fujimoto, Science **254,** 1178 (1991).
5. M. D. Fox, IEEE Trans. Sonics Ultrason. **SU-25,** 281 (1978).
6. D. P. Davé and T. E. Milner, Opt. Lett. **25,** 1523 (2000).
7. V. L. Newhouse, E. S. Furgason, G. F. Johnson, and D. A. Wolf, IEEE Trans. Sonics Ultrason. **SU-27,** 50 (1980).
8. H. Ren, K. M. Brecke, Z. Ding, Y. Zhao, J. S. Nelson, and Z. Chen, Opt. Lett. **27,** 409 (2002).
9. D. Piao and Q. Zhu, "Quantitation of Doppler angle and flow velocity mapping by combining Doppler shift and Doppler bandwidth measurements in optical Doppler tomography" Appl. Opt. (to be published).
10. D. Piao, L. Otis, N. K. Dutta, and Q. Zhu, Appl. Opt. **41,** 6118 (2002).
11. R. Wolfram-Gabel and H. Sick, Cells Tissues Organs **164,** 102 (1999).

April 15, 2002 / Vol. 27, No. 8 / OPTICS LETTERS 607

Rotary mirror array for high-speed optical coherence tomography

Nan Guang Chen and Quing Zhu

University of Connecticut, Department of Electrical and Computer Engineering, Storrs, Connecticut 06269

Received November 9, 2001

We have developed a simple, high-speed, high-duty-cycle, linear optical delay line suitable for optical coherence tomography and optical Doppler tomography. Periodic longitudinal scanning is achieved by use of a tilted mirror array rotating at a constant speed. With a typical motor speed of 4000 rpm, our system has demonstrated a 2-mm axial scanning range, a 2400-Hz repetition rate, 94% duty cycle, and less than 0.1% nonlinear errors. Much higher repetition rates can be readily achieved by use of high-speed motors. © 2002 Optical Society of America

OCIS codes: 110.4500, 170.3880, 120.5800, 220.4830.

Optical coherent tomography (OCT) permits exceptionally high-resolution subsurface imaging of tissue microstructures. Optical Doppler tomography is an extension of OCT, and it tracks Doppler shifts arising from the moving scatterers inside blood vessels. In many clinical situations, successful use of OCT and optical Doppler tomography depends on the design of fast delay lines, which can provide real-time imaging and, therefore, suppression of motion artifacts. Parameters associated with the design of fast delay lines are scanning range, linearity, duty cycle, and cost. Often, compromises among these parameters have to be made.

A primitive delay line is a translating mirror, which is driven by a linear motor, an actuator, or a piezoelectric transducer. As the mirror moves back and forth, the power consumption required for generating acceleration increases dramatically with frequency and scanning range. This increase is the reason that most commercially available linear motors and actuators can provide a repetition rate of only ~30 Hz when a 2–3-mm scanning range is required.[1] Although piezoelectric transducers can be driven at much higher frequencies, they can provide only a limited scanning range. Resonant scanners have been demonstrated to achieve a frequency of 1200 Hz and as great as 3-mm optical length difference.[2] The drawback to resonant scanners is that the optical path-length change is a time-dependent sinusoidal function. As a result, the Doppler frequencies of interference signals are depth dependent and vary within a wide range, which may cause difficulties in signal filtering and introduction of more noise. More-sophisticated delay lines convert a small-angle rotation into a longitudinal optical path-length change. This conversion can be achieved by use of either a retroreflector[2] or a combination of gratings and lenses.[3,4] The former implementation requires a complicated arrangement of mirrors and lenses and precise alignment. Grating-based delay lines have the flexibility to adjust group delay and phase delay independently. Repetition rates of 2000 (Ref. 3) and 4000 (Ref. 4) scans/s have been reported for such delay lines with a galvonometer (driven with a 1-kHz triangle waveform) and a 4-kHz resonant scanner, respectively. It appears that without resonant scanners, vibrational motion–based mechanical scanning cannot readily achieve a speed high enough to meet real-time data acquisition requirements. It is a great idea to use rotational motion–based devices instead of vibrating devices to generate optical path-length scanning. Once a steady rotation speed has been reached, a small amount of energy is required for maintaining rotation speed. Rotating cubes,[5,6] rotating roof prisms,[7] and a combination of a polygonal mirror and a glass cube[8] can scan up to 28.5 kHz. However, these methods suffer from rather low duty cycles and (or) considerable nonlinearity of optical path-length change. Recently, an OCT system without any moving parts for depth scanning was proposed,[9] and a high-repetition scanning rate of 500 kHz was achieved in a scanning range of 25 mm by use of optical frequency comb generators. However, the depth resolution (100 μm) and signal-to-noise ratio of this system need to be improved. In addition, the cost of this system is high because of the use of expensive components, such as gigahertz electronics and electro-optical modulators.

In this Letter we present a novel design for implementing a periodic modulation of the optical path length in the reference arm, which consists of a dc motor, a mirror array, and a convex lens. We use a regular motor with a speed of 4000 rpm in our current OCT system to demonstrate the feasibility of real-time scanning with our new design. As many as 2400 A lines were acquired every second in a 2-mm range, without noticeable nonlinear effects. A much higher scan rate can be readily obtained by replacement of our current motor with high-speed motors, e.g., with speeds of 20,000–100,000 rpm.

The principle of our delay line is quite simple, as is illustrated in Fig. 1. Shown in Fig. 1(a) is a segment of an infinite linear mirror array. Mirrors are deployed uniformly on a planar base. Their reflective facets are tilted at a small angle α with respect to the base. The optics of the reference arm is arranged so that the reference beam hits a mirror surface perpendicularly and is reflected back along the same path into the optical fiber. When the mirror array moves at a

0146-9592/02/080607-03$15.00/0

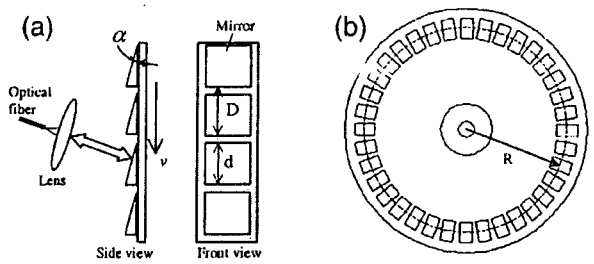

Fig. 1. (a) Optical delay line with a section of an infinite linear mirror array. (b) Rotary mirror array derived from the linear array.

constant speed v, the optical path length will be modulated periodically. Within each period, the change of optical path length is a linear function of time. The scanning range, ΔL, and speed v_l are given by

$$\Delta L \approx d \sin \alpha , \tag{1}$$

$$v_l = v \sin \alpha , \tag{2}$$

respectively, where d is the length of the mirror in the direction of movement. The repetition rate is inversely proportional to the spatial period D:

$$f = v/D . \tag{3}$$

Of course, an infinite mirror array is not practical. However, one can make a local approximation by bending a section of an infinite linear mirror array into a ring [see Fig. 1(b)], forming a circular array of discrete rotational symmetries. When the mirror array rotates at a constant angular speed ω, the linear translation speed at the light-illumination point is $v = \omega R$, where R is the equivalent radius. In each duty cycle, the one-way optical path length can be expressed as a function of time δt with the origin at the moment when the incident beam illuminates the center of the mirror:

$$\begin{aligned} \Delta l &= R \sin \alpha \sin(\omega \delta t) \\ &\approx R \sin \alpha [\omega \delta t - (\omega \delta t)^3/6]. \end{aligned} \tag{4}$$

Since the rotation angle $\omega \delta t$ is approximately in the range $[-d/2R, d/2R]$, the maximum value of the relative nonlinear error is approximately $d^2/24R^2$, which is as small as 0.1% for our experimental system (R = 50 mm and d = 8.2 mm). To the best of our knowledge, this has never been achieved by other mechanical fast-scanning devices.

A schematic diagram of our fast OCT system is shown in Fig. 2. A superluminescent LED (SLED1300S5A, Opto Speed) is used as low-coherence source and yields better performance than the erbium-doped fiber amplifier used in our previous system.[10] The center wavelength and the −3-dB bandwidth are 1300 and 40 nm, respectively, resulting in a coherence length of 18.6 μm. The typical output power of the system, ~2.5 mW, is coupled into a single-mode optical fiber. A 2 × 2 optical coupler distributes input light evenly into the reference and the sample arms. In the reference arm, longitudinal scanning over a 2-mm range is achieved with our rotary mirror array. The mirror array consists of 36 identical small mirrors tilted at a 14° angle with respect to the base plane and the direction of the local linear velocity. The equivalent radius R is 50 mm, and D is ~8.7 mm for each mirror. A fairly high duty cycle of 94% was measured, in good agreement with the theoretical prediction. The mirror array is directly driven by a permanent magnet dc motor (GNM 2636A, MicroMo Electronics). The maximum continuous speed of the motor is 4000 rpm, which provides a repetition scanning rate of 2400 Hz. At the sample arm, a galvanometer scans the light beam laterally on a sample to yield two-dimensional images. We use a 10-Hz sawtooth waveform to drive the galvanometer so that a B scan, consisting of 240 A lines, can be acquired in 0.1 s. Reflections from both arms are superimposed at the output fiber, and then the interference signals are detected by a low-noise photodetector (D400FC, Thorlabs). Since the original interference signals have a center frequency of ~7.8 MHz , we used a heterodyne detection scheme to reduce the speed requirement on a digitizer. The heterodyned signals (~300 kHz in center frequency) are converted to digital signals by a PCI data acquisition card (PCI-MIO-16E-1, National Instruments). Further signal processing and A-line segmentation are conducted by a personal computer. We used a reflective optical sensor together with a mark on the periphery of the rotating base to generate feedback signals for timing purposes. With such an arrangement (not shown in Fig. 2), individual A lines can be selected from continuous waveforms with high accuracy and repeatability.

To validate our new design, we conducted a series of imaging experiments. In one experiment, a small piece of transparent film fixed upon a glass plate served as a simplified sample. The thickness of the transparency film was 127 μm, and a 255-μm gap existed between the back surface of the transparent film and the glass plate [Fig. 3(a)]. Shown in Fig. 3(b) is a cross-sectional image acquired with the setup given

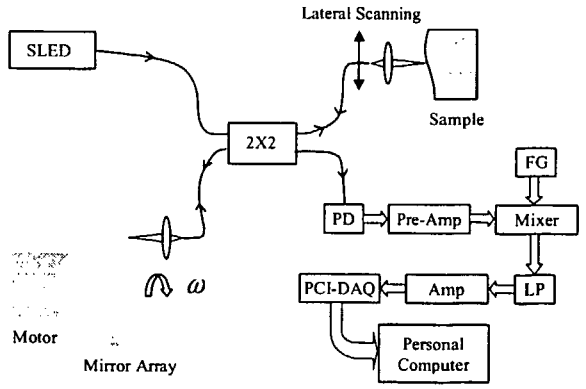

Fig. 2. Schematic diagram of our fast OCT system. SLED, superluminescent LED; PD, photodetector; Pre-Amp, pre-amplifier; FG, function generator that supplies reference signals of ~7.5 MHz; LP, low-pass filter; Amp, amplifier; PCI-DAQ, PCI data acquisition card.

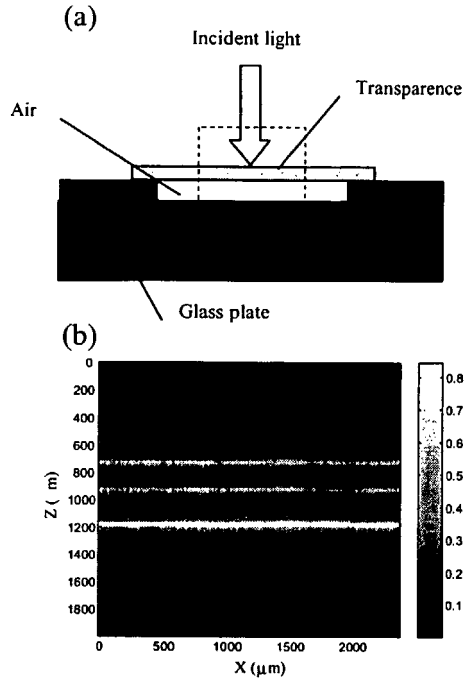

Fig. 3. (a) Simple sample for imaging. The dashed square indicates the imaging area. (b) Cross-sectional image acquired with our fast OCT system.

in Fig. 2. The interfaces of the transparent film and the glass plate with the air can be identified clearly. The refractive index of the transparent film is 1.55, so the thickness that appears in the image is 196.5 μm.

The advantages of our fast-scanning delay line over existing technologies are numerous. First, video-rate image acquisition can be readily achieved. We are planning to use a high-speed motor (~20,000 rpm) in the next version of the OCT system. As a consequence, an ~12-kHz scan rate will be obtained. If 300–400 A lines are used for one B scan, the imaging frame rate will range from 30 to 430 frames/s. Although this speed is adequate for most clinical applications, there are no mechanical difficulties in rotating the mirror array at an even higher speed. The practical speed will be limited only by the light-source power and the signal-to-noise ratio of the entire system. The scanning range can be extended to 3 mm by a slight increase in the size of the mirror array. Second, since the optical path length is modulated in a linear fashion, the frequencies of interference signals are depth independent and are limited to a relatively narrow band. These features are highly desirable for optical Doppler tomography. In addition, a narrow-band filter can be used to achieve a high signal-to-noise ratio. Third, the duty cycle of our system is high, and a duty cycle of more than 94% is feasible. Fourth, in setting up and maintaining high-speed rotation, much more energy is saved than in vibrating devices. Mechanical vibrations and noises can also be reduced. Finally, our delay line does not suffer from group-velocity dispersion, which is desirable for retaining spatial resolution.

In conclusion, we have demonstrated a novel design for a high-speed optical delay line for OCT systems. A repetition scan rate of 2400 Hz over a 2-mm range has been achieved with our prototype system. Excellent linearity and high duty cycles are obtained. We are quite confident that much higher speed can be readily achieved with high-speed motors, so that images can be acquired at a video rate. The application of this delay line will not necessarily be limited to OCT. In fact, it can replace many fast delay lines used in a variety of optical systems.

We thank graduate student Daqing Piao for his help with the optical system setup. We thank the U.S. Department of Defense Army Breast Cancer Program (grants DAMD17-00-1-0217 and DAMD17–01-1-0216) and the National Institutes of Health (grant NIH 1R01 DE11154-03) for their funding support. N. G. Chen's e-mail address is chenng@engr.uconn.edu.

References

1. J. M. Schmit, IEEE J. Sel. Top. Quantum Electron. **5,** 1205 (1999).
2. R. Windecker, M. Fleischer, B. Franze, and H. J. Tiziani, J. Mod. Opt. **44,** 967 (1997).
3. G. J. Tearney, B. E. Bouma, and J. G. Fujimoto, Opt. Lett. **22,** 1811 (1997).
4. A. M. Rollins, M. D. Kulkarni, S. Yazdanfar, R. Ung-arunyawee, and J. A. Izatt, Opt. Express **3,** 219 (1998), http://www.opticsexpress.org.
5. C. B. Su, Opt. Lett. **22,** 665 (1997).
6. J. Szydlo, H. Bleuler, R. Wälti, and R. P. Salathé, Meas. Sci. Technol. **9,** 1159 (1998).
7. H. Harde and H. Burggraf, Opt. Commun. **38,** 211 (1981).
8. N. Delachenal, R. Wälti, R. Gianotti, S. Christov, P. Wagner, R. P. Salathé, U. Dürr, and G. Ulbers, Opt. Commun. **162,** 195 (1999).
9. S. J. Lee, B. Widoyatmoko, M. Kourogi, and M. Ohtsu, Jpn. J. Appl. Phys. **8B,** L878 (2001).
10. D. Q. Piao, Q. Zhu, N. Datta, S. K. Yan, and L. Otis, Appl. Opt. **40,** 5124 (2001).

A DSP-based real-time optical Doppler tomography system

Shikui Yan, Daqing Piao, Yueli Chen and Quing Zhu

Electrical & Computer Engineering Department, University of Connecticut, CT 06269-2157

Abstract: In this paper, we present a real-time data processing and display unit based on a custom designed digital signal processor (DSP) module for tissue structure and Doppler blood flow imaging. The DSP module is incorporated into a conventional optical coherent tomography (OCT) system. We also demonstrate the flexibility of embedding advanced Doppler processing algorithms in the DSP module. Two advanced velocity estimation algorithms previously introduced by us are incorporated in this DSP module. Experiments on intralipid flow demonstrate that this DSP system is capable of imaging pulsatile flow at a rate of several hundred pulses per minute. *In vivo* imaging capability with pulsatile blood flow is also demonstrated.

OCIS codes: (170.0170) Medical optics and biotechnology; (170.4500) Optical coherence tomography.

Correspondence: Prof. Q. Zhu, University of Connecticut, Storrs, CT 06269; e-mail Zhu@engr.uconn.edu; fax: 860-486-1273.

1. Introduction

Optical Doppler tomography (ODT) [1, 2] is a noninvasive, noncontact imaging modality that combines coherent gating and Doppler principle to obtain high-resolution cross-sectional imaging of tissue microstructure and blood flow, simultaneously. As a functional extension of optical coherence tomography (OCT), [3] ODT performs depth-resolved tomographic flow measurements in a series of time frames. Since ODT imaging is highly localized, the image acquisition speed must exceed the time scale of the movement of non-stationary objects in order to avoid motion artifacts. In addition, a real-time ODT data processing scheme providing rapid and continuous imaging and monitoring of blood flow synchronized with structural imaging is needed for timely diagnosis. The development of rapid-scanning optical delay line is the first technical challenge for real-time ODT, and it is practically solved. [4, 5, 6] The second issue is the development of real-time data processing and display unit. In general two steps of data processing are involved in simultaneous structure and flow velocity detection using ODT. First, a structural cross-sectional image is obtained by segmenting the raw interference data to obtain individual A-line profiles, and mapping the amplitude of each A-line profile to a series of fixed gray scales. Second, a flow image is obtained using Doppler analysis and displayed either aside or overlapped on top of the structural image for simultaneous visualization of flow regions and flow directions. The structural image formation is straightforward and fast in general by using Hilbert transform and envelope detection. The flow imaging however, requires intensive computations.

Because of ODT's promising potential in clinical applications, real-time ODT is under extensive investigations. Westphal et al. and Rollins et al. have employed autocorrelation scheme in

hardware to measure the phase of the correlation function, which corresponds to the local Doppler shift. [7,8] Zhao et al have proposed a method utilizing the polarization properties of light to obtain phase information and the method was implemented by optical Hilbert transformation. [9, 10] Yang, et al. have implemented in-phase and quadrature (I & Q) demodulator in hardware and subsequent Kasai autocorrelation velocity estimator in software.[11] All these techniques focus on the hardware-implementation of a particular Doppler algorithm in order to eliminate the need of off-line processing of the recorded interference signals. The implemented Doppler algorithm, therefore determines the performance of the velocity estimator.

The Doppler analysis algorithms currently used in ODT can be classified into three major categories: a short-time Fourier transform (STFT) [1] method, a filtering method, [12] and a Hilbert transform [13] method. The short-time Fourier transform method extracts local Doppler shifts by measuring the spectrum centroid displacement of the interference signal. The filtering method directly maps the frequency shift at each pixel using digital filtering technique performed by a bank of narrow band-pass filters. The Hilbert transform method, also called correlation method, calculates the autocorrelation of individual A-scan line or cross-correlation between sequential A-scan lines, and estimates velocity changes from the phase of the correlation function. The STFT method is efficient in computation for its simplicity, but it is noisy. The filtering method is robust to noise and most accurate compared with STFT and Hilbert transform techniques, however its digital filtering process requires intensive computation. The Hilbert transform method is known to have highest velocity sensitivity when cross-correlation is taken between sequential A-lines. Nevertheless it is noisy at lower flow speed and/or lower signal-to-noise-ratio (SNR) region because correlation techniques are more sensitive to local decorrelation of the

flow field resulting from low SNR or high velocity gradient that is present at low flow velocity region. [12, 14] The Hilbert transform method is computational intensive due to the correlation process. An investigation on the off-line computation load of these three categories of algorithms reveals that the flow image processing of a typical data set of 512*2048 requires approximately 15, 60, and 106 seconds for the three algorithm categories, respectively, on a Pentium III 800MHz-based PC. [12]

In the above-mentioned real-time ODT techniques primarily the Hilbert transform is implemented. Hilbert transform accomplished in hardware has the advantage of simple implementation, however, it lacks the flexibility when a different Doppler method is about to use. An ODT system based on DSP module, on the other hand, has the advantage of embedding any desired high-performance Doppler algorithm. In addition, it has the flexibility of incorporating other functional imaging algorithms such as spectroscopic OCT. [15] In this paper, we present a real-time ODT system using a low-cost digital signal processor (DSP) module embedded with two advanced Doppler algorithms. In this approach, a custom-designed DSP is incorporated into a conventional ODT system with a grating-based rapid scanning delay line. Configured with a signal processing evaluation module and an analog-to-digital (AD) daughterboard, this DSP performs data acquisition, structural imaging, and flow processing sequentially. DSP performance evaluation indicates the real-time data processing capability. Experiments on intralipid flow demonstrate that this DSP system is capable of imaging pulsatile flow at a rate of several hundred pulses per minute. *In vivo* blood flow imaging with pulsatile flow is also demonstrated. Two advanced velocity estimation algorithms, namely weight centroid

and digital filtering, are embedded in this DSP, and the superior performance of the sliding-window filtering algorithm is also demonstrated.

2. The flow velocity estimation algorithms embedded in DSP

In our previous work, [12] we discussed five velocity estimation algorithms, among which we introduced two new techniques: weighted centroid and sliding-window filtering. We also presented a quantitative assessment of the velocity estimation accuracies of these algorithms by simulations and *in vivo* study. These comparisons have shown that the weighted centroid technique slightly outperforms other three currently available algorithms. The sliding-window filtering technique is demonstrated to be superior to all other techniques on velocity estimation accuracy, most significantly at low signal-to-noise ratio (SNR). In terms of operational count, however, the computation time of sliding-window filtering method is 6 times higher than weighted centroid method. To take the advantage of the robust sliding-window filtering technique on flow estimation and also satisfy the real-time data processing demand, we have implemented a low-cost DSP-based signal processing module. This DSP module improves the calculation speed dramatically such that real-time data processing is readily achieved. In the following section, we give a brief review of these two algorithms that are embedded in the DSP.

Since ODT requires a broader bandwidth to detect frequency shifts due to moving scatterers, averaging of repeated data acquisition to improve SNR is necessary. By taking into account the averaging, we express the detected two-dimensional (2-D) interference signal after Hilbert transform as [12]

$$\tilde{z}_{k,i}(t) = |\tilde{z}_{k,i}(t)|\, e^{j\omega t} \qquad (1)$$

where t is the time argument along the depth scanning direction, k represents the lateral dimension of the k th A-line, i is the index of the repeated A-line measurements, and ω is the angular frequency of signal reflected from the target. The sampled interferometric signal is represented by $\tilde{z}_{k,i}(t_n)$, where $t_n = nt_s$ and t_s is the sampling interval, and the power spectrum of $\tilde{z}_{k,i}(t_n)$ is denoted with $P^n{}_{k,i}(\omega)$.

2.1 Weighted centroid algorithm

The weighted centroid algorithm, which is an extension of the conventional centroid method, is given by

$$\overline{\omega}_{k,i}(n) = \int_{-\infty}^{\infty} \frac{\omega[P^n{}_{k,i}(\omega)]^{\xi} d\omega}{[P^n{}_{k,i}(\omega)]^{\xi} d\omega} \qquad (2)$$

where a positive integer ξ is introduced as the weight of the spectrum to emphasize the frequency component corresponding to the peak power in the spectrum.

2.2 Sliding-window filtering algorithm

The sliding-window filtering technique directly maps the frequency shift at each pixel using a digital band-pass filtering. In this approach, the detected signal $\tilde{z}_{k,i}(t_n)$ at each depth scanning range t_n is processed by a filter bank consisting of M filters, f_1, f_2, ..., f_M, yielding one signal at the output of each filter as illustrated in Fig. 1. This produces M output signals $\tilde{O}_m(t_n)$, $m = \{1, 2, ..., M\}$ for each detected signal such that

$$\tilde{O}_m(t_n) = \tilde{z}_{k,i}(t_n) \otimes F^{-1}(f_m) \qquad (3)$$

where the passband of f_m is $[(2m-1)\pi/2M - \Delta\omega/2, (2m-1)\pi/2M + \Delta\omega/2]$ with $\Delta\omega$ being the filter bandwidth. The output signals represent components of input signal that change at a rate corresponding to the passband of the filter. Then, at each range t_n, the energy in each filter, $\varepsilon_m(t_n)$, is estimated as [16]

$$\varepsilon_m(t_n) = \sum_{t'=t_n-\Delta t/2}^{t_n+\Delta t/2} \left[\tilde{O}_m(t')\right]^2 \qquad (4)$$

where Δt represents a short range window centered at t_n. At any given t_n, the filter window position corresponding to the maximum $\varepsilon_m(t_n)$, $m = \{1,2,...,M\}$, represents the most significant frequency component, equivalently the frequency shift, of flow signal. The filtering window $[\omega_1, \omega_2]$ determines the velocity resolution of this algorithm, and a better resolution requires a narrower filtering window. However, a robust estimate of the velocity requires a broader filtering window. A compromise between velocity resolution and robustness to noise has been achieved by using a bandwidth of $\pi/32$ when a 2nd order Chebyshev filter of the first kind is chosen.

3. The architecture of DSP-based ODT system

The DSP-based ODT system is constructed on top of a conventional ODT device. [17] Functionally, this new system consists of four units (shown in Fig. 2): ODT scanner, control signal generator, embedded real-time processor, and image display module. The detailed function of each unit is described as follows.

Unit 1. ODT scanner

The ODT scanner is a typical balanced setup configured with one 1×2 and one 2×2 fiber couplers (see Fig.3). The low coherence source is a superluminescent diode with 1300 nm center wavelength, 40 nm spectral width, and 2.0 mW maximum output power. In the reference arm, a scanning optical delay line based on Littrow-mounting of diffraction grating is used to generate range scanning and a phase modulation for carrier frequency as well. [12] In the sample arm, a galvanometer and an achromatic lens are integrated to perform repeatable lateral scanning that is essential for continuous monitoring of flow. In the detection arm, the signal is detected differentially by an auto-balanced receiver, with which the source intensity noise is rejected. The signal is then amplified, bandpass filtered and digitized.

Using this system, cross-sectional imaging of one frame per second is obtained by driving reference arm and sample arm galvanometers with 128 Hz triangle wave and 1Hz sawtooth wave, respectively. The reference galvanometer is capable of scanning at much higher frequency, however, 128 Hz scan speed is used due to the bandwidth limitation of the dual-balanced receiver. Each frame consists of 128 axial scans containing 2048 data points at each round of scan. Because we used 50% duty cycle of galvanometer scanning, each A-line covers 1024 points, and 4 consecutive A-lines are then averaged to improve the SNR. In the axial dimension, 16 points are averaged at one pixel, resulting pixel dimension of 64×32 covering an area of 2.5mm×1.0mm (intralipid study) and 2.5mm×2.0mm (rat study).

Unit 2. Control signal generator

To synchronize the axial scanning, lateral scanning as well as data acquisition, we have built a control signal generator based on a National Instruments (NI) multi-function Data Acquisition

(DAQ) card, PCI-MIO-16E-1. As described in Fig. 4, this unit generates synchronization signals for ODT scan and data acquisition: one fast triangle wave for reference arm scanning and one slow sawtooth wave for lateral scanning as previously mentioned, and a TTL-compatible triggering signal for data acquisition and real-time processing.

Unit 3. Embedded real-time processor

Shown in Fig. 5 (a) is the newly embedded real-time module that is a combination of TMS320C6701 DSP Evaluation Module ('C6701 EVM, Texas Instruments Inc.) [18-20] and analog expansion daughterboard AED-109 [21] (Signalware Inc.). The 'C6701 EVM board is a complete DSP system based on 'C6701 DSP chip operating up to 1336 million instructions per second (MIPS) with a CPU clock rate of 167 MHz. With 'C6701 one can actually perform two multiplication and accumulation operations within a single clock cycle. This board also provides 256 KB of external 133-MHz synchronous burst static RAM (SBSRAM) and 8 MB of external 100-MHz synchronous dynamic RAM (SDRAM), both of which could be used as data buffers. The daughter board AED-109 has two dual-channel 12-bit A/D converters with up to 8-MHz sampling speed and two D/A converters; the input channels have been configured into differential inputs for higher SNR consideration. In addition to analog channels, 16-buffered digital signals can be used as flags for system control.

The data flow with this real-time processor is shown in Fig. 6. When ODT scanning starts, the daughter board AED-109 acquires the signal from the ODT scanner, and the 12-bit data is buffered into 256-word two-way FIFO in the field programmable gate array (FPGA) XCV100E6 (Xilinx Inc.). As soon as this FIFO is full, XCV100E6 triggers 'C6701 DSP to transfer data to

'C6701 in direct memory access (DMA) mode. The circular buffer in the 'C6701 DSP memory, which is segmented into 8 frames with 256 words per frame, can hold 2K words data acquired during one complete fast scanning. The transferred 256-word data is saved into one frame of circular buffer, then the circular buffer is polled to process the new coming data. For structural image formation and flow calculation using weighted centroid algorithm, this DSP module processes each section (256 words) in the circular buffer continuously; however, for flow calculation using sliding-window filtering algorithm, DSP needs to acquire 4 continuous frames before it starts to process 1024 data points for a complete A-scan line. The processed structural image and flow image data are saved into each buffer in the SDRAM on 'C6701 EVM. The next step is to load image data into PC for display.

Unit 4. Image display module

A real-time image display is the last, yet critical step of this real-time DSP-ODT system. The real-time data exchange (RTDX) provided by Texas Instruments Inc. offers continuous bi-directional data exchange in real time with minimal perturbation to the application. However, in 'C6701 EVM, the maximum RTDX rate is 20 Kbytes/second. Since structural image and flow image data are in floating data format (4 bytes), a total of 96 Kbytes data needs to be loaded in one image frame (1 second) for simultaneous display of both structural and flow images, which is beyond the RTDX speed of our current DSP. To overcome this problem, the host-port interface (HPI) between DSP and PC is employed to load image data right after processing. With this technique, flow image processing and image uploading are performed alternately. During the operation DSP is continuously processing and saving image data into 8 Mbytes SDRAM on 'C6701 EVM to avoid data loss. After DSP has completed desired frames, all of the image data

are loaded at one time. This strategy assures the image acquisition speed up to a maximum of 128 A-scans per frame, which is the actual scan speed. If a photo-receiver with broader bandwidth is employed in ODT scanner to accommodate faster scanning, and a new high-speed RTDX (HS-RTDX) with 2 Mbytes/second transfer rate is implemented, we expect to achieve much higher processing and display updating speed than current 1 Hz frame rate.

4. Evaluation of DSP performance

To study the performance of the introduced DSP, we estimated the DSP cycles of three processing modes: structural image, weighted centroid flow image and sliding-window filtering flow image. The resulting operational structures for implementing each of them are shown in Fig. 7 and are described in the following paragraphs.

For structural image, one set of A-scan line with 1024 data points is segmented uniformly into 64 sections, with 16 points per section. The data in each section is then Hilbert transformed by floating-point FFT and IFFT pair. For each section, the maximum of the absolute values of Hilbert transformed data is determined, which represents the signal level in the local pixel. Therefore, a total of 64 pixel values are obtained for single A-scan data in structural imaging. The most calculations are FFT and IFFT pairs, resulting 0.043M cycles for fixed-point calculation and 0.041M cycles for floating-point calculation.

For weighted centroid algorithm, again, one set of A-scan line is segmented into 64 sections. The data in each section is zero-padded to 64 points, and then Fourier transformed by 64-point complex floating-point FFT. From the calculated 32-point spectrum value of each section, the

Doppler frequency shift is calculated by finding the local center frequency with weighted centroid principle and subtracting the known modulation frequency. Again, a total of 64 Doppler shift values are obtained for single A-scan data in flow imaging by weighted centroid technique. The most calculations focus on FFT. By using complex radix-2 floating point FFT, about 0.096M cycles are needed to finish the calculation of one 1024-point A-scan data. If complex radix-4 fixed point FFT is implemented instead, only 0.077M cycles are needed.

For sliding-window filtering algorithm, a complete set of A-scan line with 1024 data points is filtered individually by 32, 2nd order IIR bandpass filters, each of which has one of 32 evenly distributed narrow passbands from 0 to π, and the passbands of all filters cover the entire spectrum. The filtered 1024 data is segmented into 64 sections equally, with 16 points per section. In each section, the filter number corresponding to the maximum signal power after these 32 filters is indexed as the center frequency, and the Doppler shift is calculated by subtracting the modulation frequency. The resulted total number of Doppler shift values for single A-scan data in sliding-window filtering method is 64. The most calculations are IIR filtering banks. The execution takes about 0.32M cycles for 1024-point fixed-point calculation, and 0.61M cycles for floating point calculation. As listed in Table 1, the most intensive calculation is on sliding-window filtering technique, which is about 6 times as that of weighted centroid technique. Nevertheless, for one A-line at a duration of 1/128 second, the computation load of all three modes are within the 1.3M cycles real-time limitation of the167MHz 'C6701 EVM.

The above-described DSP speed estimation is based on the approximation that the DSP has enough internal memory. However, 'C6701 DSP provides only 64 Kbytes internal memory for program storage and 64 Kbytes internal memory for data storage. As a result, the relatively low speed external memory in SBSRAM and SDRAM has to be used for DSP object file because it has a size of 95 Kbytes, which exceeds the 64 Kbytes internal program memory. If a code is present in an external memory, more cycles are demanded for its execution. In addition, a large amount of data buffers are needed in external memory. By optimizing memory allocation and code efficiency, we have achieved continuous calculation for simultaneous structural and flow imaging in less than 1 second with the current DSP module.

To verify that our DSP code is efficient, we have evaluated the ratio of DSP speed for two flow processing modes and compared it with Matlab calculations. In Matlab, 2.5 seconds and 17 seconds are needed for weighted centroid technique and sliding-window filtering technique, respectively, on a Pentium-4 2.0GHz PC. The ratio of speed in Matlab is 6.8, which is very close to 6.4 achieved by 'C6701 DSP using floating-point calculation.

'C6701 is a floating point DSP, and it can operate in either fixed-point or floating-point calculation. 'C6701 uses 2-byte short date type in fixed-point FFT and IIR functions; and 4-byte floating data type in floating-point FFT and IIR functions. Because Matlab uses 8-byte double data type to do the calculation, we can use the result from Matlab as a benchmark, and the calculation accuracy of fixed-point and floating-point can be found by studying the mean-square-error (MSE) with respect to the Matlab results. Table 2 lists the MSE in DSP calculation for fixed-point and floating-point data types. By comparing Tables 1 and 2, we can see that there is

a trade-off between speed and calculation accuracy on choosing either fixed-point or floating-point DSP. Since our DSP system is able to process flow information in desired time frame, the floating-point DSP is favorable for its higher accuracy and is therefore implemented in our code.

5. Results

5.1 Experimental flow

To demonstrate the performance of our DSP-ODT system, we constructed experimental flow setup with 0.5% intralipid solution. The ODT probing-beam is focused to the axis of a glass capillary tubing with 1.0mm inner diameter, 1.2mm outside diameter and 100mm in length. The glass capillary is mounted to a rotary stage, and connected to a 2-meter long 3/32″ plastic tubing. The mean flow velocity of intralipid through the glass capillary tubing is converted from the time interval of liquid traveling 1 meter distance in the 3/32″ plastic tubing that is placed straightly on a horizontal plane. A peristaltic tubing pump is used to drive the intralipid through the capillary tubing and circulate it in the tubing loop. The pulsation induced by peristaltic pumping is used to emulate the *in vivo* blood circulation. The tubing pump gives approximately 3 pulses per second at its minimum rotation speed.

Using this setup, 30 frames are taken continuously at 1Hz frame rate. During this 30 frames interval, the pumping speed has been manually changed, with a sequence of no flow, minimum speed, gradually increased speed, gradually decreased speed, increasing/decreasing again, and stop. One frame of the real-time acquired and processed flow images is shown in Fig.8. In those flow images there are several color strips distributed perpendicular to the lateral_scanning direction in the intralipid flow region. The axial and transverse flow profiles are also plotted,

where the axial profile gives clear laminar flow pattern within single color strip corresponding to one pulse of flow, and the transverse profiles reveal the pulsation of the flow. The number of flow cycles and the magnitude of frequency shift correspond very well with the numbers of pulses generated by the pump and the speed of the flow. With this DSP-ODT system, we have captured intralipid flow of 10 pulses per second. This suggests that our system is capable of monitoring pulsatile flow circulation of human and experimental animals.

To investigate the performance of the two embedded Doppler algorithms in this real-time processing scenario, we compared the flow velocity estimation by weighted centroid technique and sliding-window filtering technique at 3 pulses per second (PPS) and 6 PPS (shown in Fig. 9). It is observed that the sliding window filtering method gives much less noisy, more accurate flow profile, and more clear pulsation pattern than weighted centroid algorithms does. This result is consistent with our simulations and experiments reported in Ref. 12.

5.2 *In vivo* study

We have conducted *in vivo* study on animal to validate the real-time imaging capability of our DSP-based ODT system. A 78-gram rat was prepared and operated under the protocol approved by the University of Connecticut (Z2400201). The blood vessels imaged were inside the opened abdomen, and the animal was euthanatized at the end of the study. 30 Frames are also taken from this rat sample, and one frame of the processed structural and flow images are shown in Figs 10. In Fig.10, the two subsurface bi-directional blood vessels are clearly identifiable. Since small blood vessels were imaged inside abdomen cavity, the color strips related to the pulsatile flow seen in intralipid experiment were not observed. This *in vivo* study indeed demonstrates

7. Acknowledgments

The authors acknowledge partial funding support from National Institutes of Health (NIH 1R01 DE11154-03). Dan Schwartz from the Animal Services of University of Connecticut is greatly appreciated for animal preparation. Shikui Yan and Quing Zhu's email addresses are skyan@engr.uconn.edu;zhu@engr.uconn.edu;

References:

1. Z.P. Chen, Y.H. Zhao, S.M. Srinivas, J.S. Nelson, N. Prakash, and R.D. Frostig, "Optical Doppler tomography," IEEE J. Sel. Top. Quant. Elect., **5**, 1134-1142 (1999).

2. J.A. Izatt, M.D. Kulkarni, S. Yazdanfar, J.K. Barton and A.J. Welch, "*In vivo* bi-directional color Doppler flow imaging of picoliter blood volumes using optical coherence tomography", Opt. Lett., **22**, 1439-1441 (1997).

3. D. Huang, E.A. Swanson, C.P. Lin, J.S. Schuman, W.G. Stinson, W. Chang, M.R. Hee, T. Flotte, K. Gregory, C.A. Puliafito, and J.G. Fujimoto, "Optical coherence tomography," Science, **254**, 1178-1181 (1991).

4. G.J. Tearney, B.E. Bouma, and J.G. Fujimoto, "High-speed phase- and group-delay scanning with a grating-based phase control delay line", Opt. Lett., **22**, 1811-1813 (1997).

5. A.M. Rollins, M.D. Kulkarni, S. Yazdanfar, R. Ung-arunyawee, and J.A. Izatt, "*In vivo* video rate optical coherence tomography", Opt. Expr., **3**, 219-229 (1998).

6. N.G. Chen, and Q. Zhu, "Rotary mirror array for high-speed optical coherence tomography," Opt. Lett., **27**, 607-609 (2002).

7. V. Westphal, S. Yazdanfar, A.M. Rollins, and J.A. Izatt, "Real-time, high velocity-resolution color Doppler optical coherence tomography," Opt. Lett., 27, 34-36 (2002).

8. A.M. Rollins, S.Yazdanfar, J.K. Barton, and J.A. Izatt, "Real-time *in vivo* color Doppler optical coherence tomography," J. Biomed. Opt., **7**, 123-129 (2002).

9. Y. Zhao, Z. Chen, Z, Ding, H. Ren, ans J.S. Nelson, "Real-time phase-resolved functional optical coherence tomography by use of optical Hilbert transformation," Opt. Lett., **27**, 98-100 (2002)

10. Z. Ding, Y. Zhao, H. Ren, J.S. Nelson, and Z. chen, "Real-time phase-resolved optical coherence tomography and optical Doppler tomography," Opt. Exp., 10, 236-245 (2002).

11. V.X.D. Yang, M.L. Gordon, A. Mok, Y. Zhao, Z. Chen, R.S.C. Cobbold, B.C. Wilson, and I.A. Vitkin, "Improved phase-resolved optical Doppler tomography using the Kasai velocity estimator and histogram segmentation," Opt. Commun., **208**, 209-214 (2002).

12. D. Piao, L. Otis, N.K. Dutta, and Q. Zhu, "Quantitative assessment of flow velocity estimation algorithms for optical Doppler tomography imaging," Appl. Opt., **41**, 6118-6127 (2002).

13. Y.H. Zhao, Z.P. Chen, C. Saxer, S.H. Xiang, J.F. de Boer, and J.S. Nelson, "Phase-resolved optical coherence tomography and optical Doppler tomography for imaging blood flow in human skin with fast scanning speed and high velocity sensitivity", Opt. Lett., **25**, 114-116 (2000).

14. P.C. Li, C.J. Cheng, and C.K. Yeh, "On velocity estimation using speckle decorrelation", IEEE Trans. Ultrason. Ferroelectr. Freq. Control, 48, 1084-1091 (2001).

15. Jian Ye, A.W. Schaefer, D.L. Marks, J.J. Reynolds, and S.A. Boppart, "Real-time processing of spectroscopic optical coherence tomography," Proceedings of IEEE International Symposium on Biomedical Imaging, TP-P1.22, Washington D.C., July 2002

16. J.R. Crowe, B.M. Shapo, D.N. Stephens, D. Bleam, M.J. Eberle, E.I. Cèspedes, C.C. Wu, D.W.M. Muller, J.A. Kovach, R.J. Lederman, and M. O'Donnell, "Blood speed imaging with an intraluminal array," IEEE Trans. Ultrason. Ferroelectr. Freq. Control, **47**, 672-681 (2000).

17. D. Piao, and Q. Zhu, "Quantitation of Doppler angle and flow velocity mapping by combining Doppler shift and Doppler bandwidth measurements in optical Doppler tomography," Appl. Opt., accepted, 2003.

18. Rulph Chassaing, "DSP Application Using C and the TMS320C6x DSK", John Wiley & Sons, Inc. 2002.

19. Texas Instrument, Inc., TMS320C62x DSP library Programmer's Reference, April 2002.

20. Texas Instrument, Inc., TMS320C67x FastRTS library Programmer's Reference, Oct 2002.

21. Signalware Co., "Documentation Package for AED-109 Multi-Channel Analog Expansion Daughterboard", Ver.1.0, Oct. 2001

Table 1. Calculation cycle evaluation of 3 processing modes based on 167MHz 'C6701 EVM.

Processing Mode	Fixed-point	Floating-point
Structural	0.043M cycles (0.26ms *)	0.041M cycles (0.25ms *)
Weighted Centroid	0.077M cycles (0.47 ms *)	0.096M cycles (0.58 ms *)
Sliding-window Filtering	0.32M cycles (1.9 ms *)	0.61M cycles (3.7 ms *)

Note: * are calculated with 167MHz system clock of TMS320C6701 EVM

Table 2. DSP calculation accuracy of fixed-point and floating point compared with Matlab calculation in 8 bytes double data format. The number is the mean square error with respect to Matlab results.

Processing Mode	Fixed-point (2-byte short)	Floating-point (4-byte float)
Structural	3.5×10^{-2}	1.5×10^{-6}
Weighted Centroid	6.8×10^{-3}	3.4×10^{-7}
Sliding-window Filtering	3.9×10^{-2}	6.1×10^{-4}

Figure captions

Fig. 1. Schematic of sliding-window filtering technique. The sliding-window filtering bank is applied to measure the components of each interference signal that change at a rate corresponding to the passband of the filters.

Fig. 2. Schematic of the DSP-based ODT system.

Fig. 3. ODT scanner, which is a typical balanced setup with both axial and lateral scanning, performed by galvanometer. O1, O2, microscope objectives; G1, G2, galvanometers; L1, L2, achromatic lenses.

Fig. 4. The synchronization strategy of ODT scanning and data acquisition.

Fig. 5. Photograph of C6701 EVM board with AED-109 daughter board plugged in.

Fig. 6. Data flow in DSP-ODT system: hardware prospective.

Fig. 7. Code structures of 3 processing modes: (a) Structural imaging; (b) Weighted centroid flow imaging; (c) Sliding-window filtering flow imaging.

Fig. 8. Experimental results on pulsatile intralipid flow. (a) 3 pulses per second; (b) 6 pulses per second.

Fig. 9. Axial and transversal velocity A-scan profiles by weighted centroid algorithm and sliding-window filtering algorithm for pulsatile intralipild flow. (a) 3 pulses per second; (b) 6 pulses per second.

Fig. 10. In vivo blood flow imaging of the abdominal blood vessels of a small rat. Two bi-directional blood vessels are clearly identified. (a) Weighted centroid flow image superimposed on structural image; (b) Sliding-window filtering flow image superimposed on structural image.

that our system is capable of monitoring *in vivo* bi-directional blood flows with reasonable sensitivity in real-time.

6. Discussions and Summary

In our DSP based ODT system, we have the flexibility of modifying system parameters that can be easily done through front panel of Labview software. The easily adjustable parameters include scanning speed of the galvanometer, the threshold in flow processing, number of averages, etc. We also have the flexibility of incorporating different flow algorithms in DSP processing module because the client program in DSP has been modularized into DAQ module, processing module and communication module. It is easy to implement new algorithms into processing module without changing the DSP code structure. Instead of implementing the DSP code in hardware, we have host program executed by Labview, which downloads DSP object file to 'C6701 EVM before the ODT system starts, and triggers DSP after initializing DSP-ODT system parameters. Therefore, any new modifications on algorithms can be easily implemented in software. The performance of this DSP system can be further improved if DSP board with higher system clock or multiple DSP boards can be employed.

In summary, we have designed a DSP-based ODT module features real-time data acquisition and processing by embedding two advanced Doppler analysis algorithms. This system incorporates a low-cost custom-designed DSP module into a conventional ODT system. Experiments of Intralipid flow and *in vivo* study have demonstrated the real-time capability of this system in capturing and monitoring pulsatile flows.

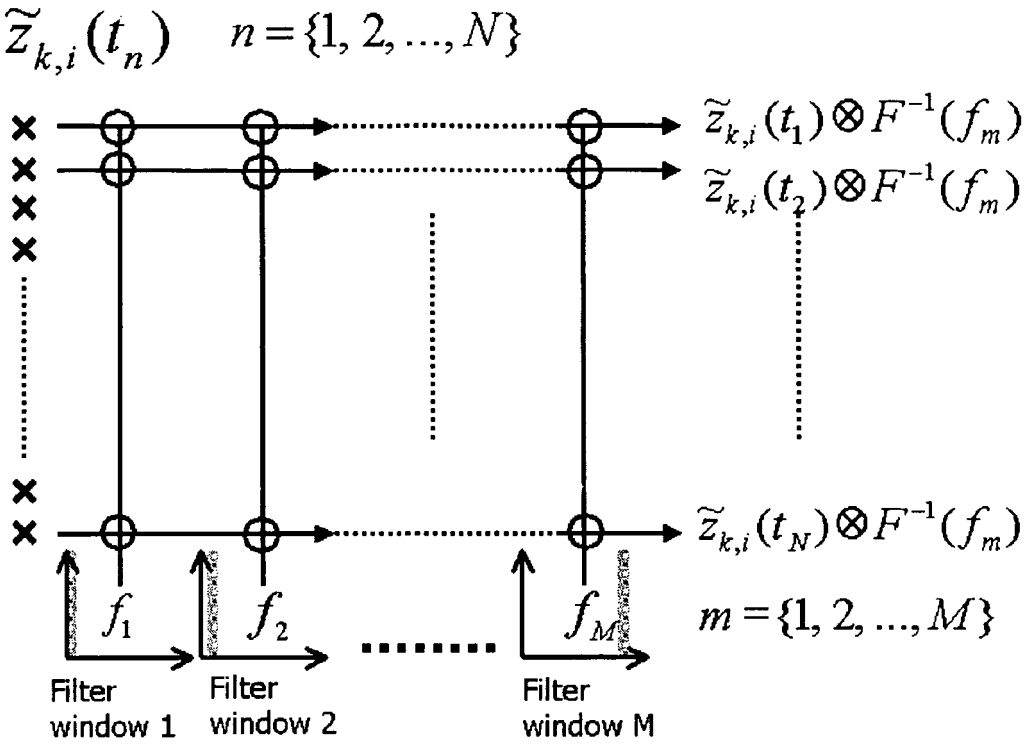
$\tilde{z}_{k,i}(t_n)$ $n=\{1, 2, ..., N\}$
$\tilde{z}_{k,i}(t_1)\otimes F^{-1}(f_m)$
$\tilde{z}_{k,i}(t_2)\otimes F^{-1}(f_m)$
$\tilde{z}_{k,i}(t_N)\otimes F^{-1}(f_m)$
f_1
f_2
f_M
$m=\{1, 2, ..., M\}$
Filter window 1
Filter window 2
Filter window M

Fig. 1

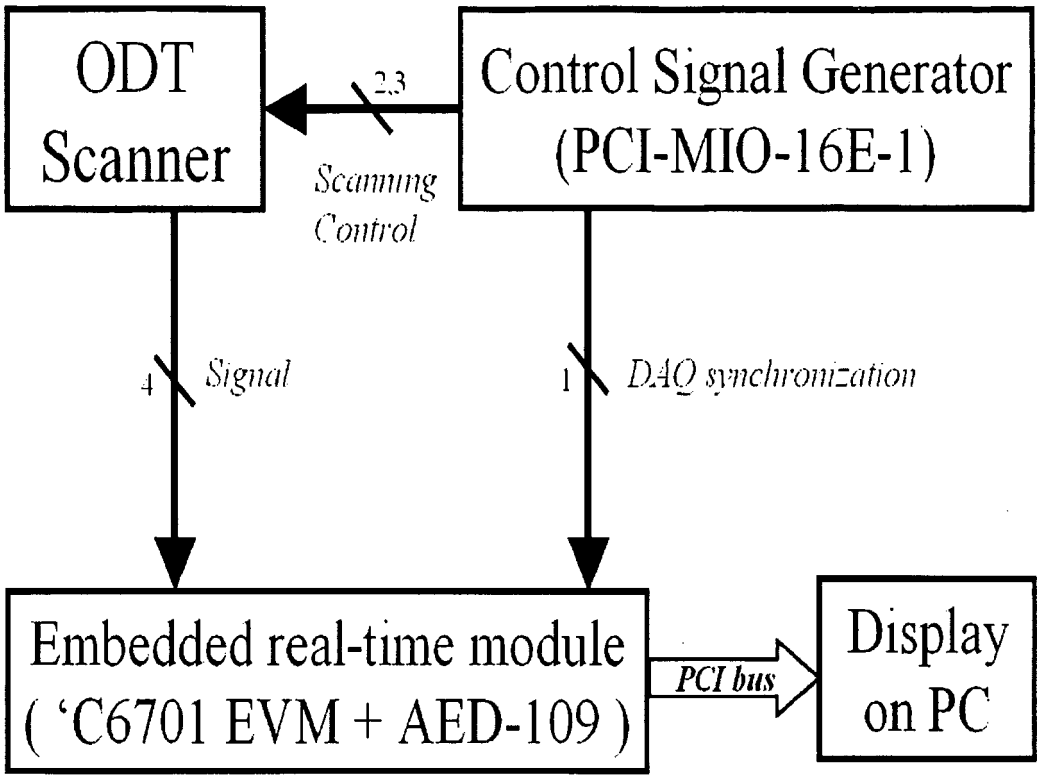
ODT Scanner
2,3
Scanning Control
Control Signal Generator (PCI-MIO-16E-1)
4
Signal
1
DAQ synchronization
Embedded real-time module ('C6701 EVM + AED-109)
PCI bus
Display on PC

Fig. 2

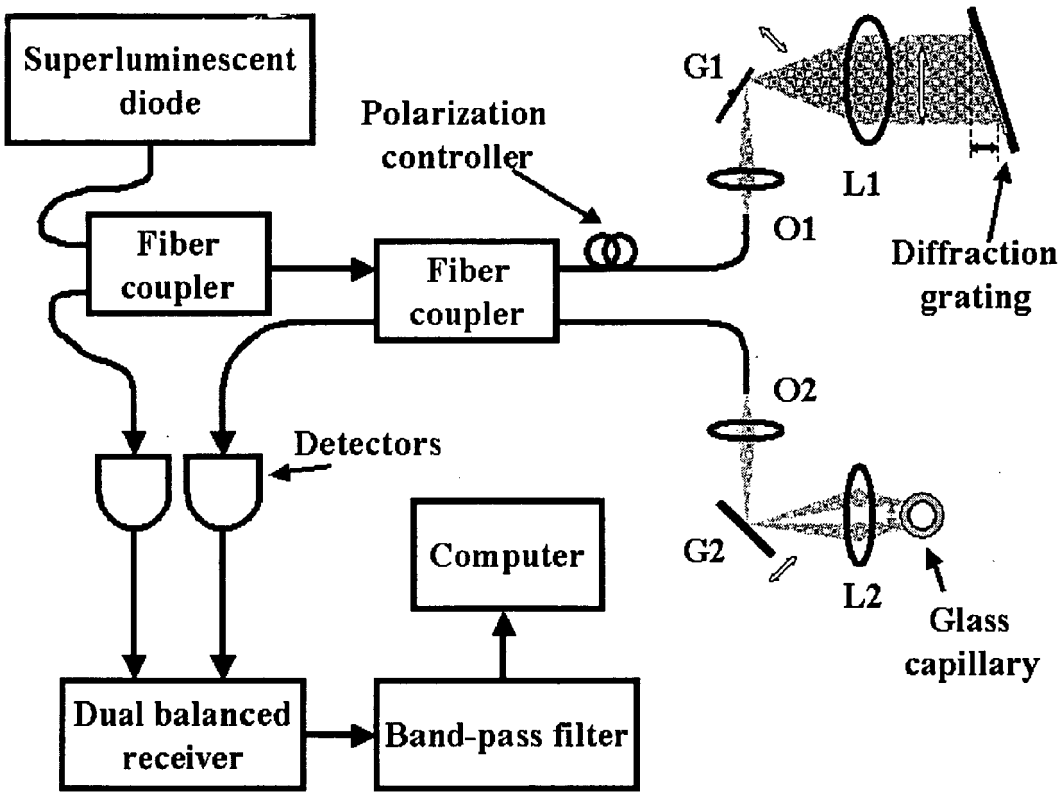
Superluminescent diode
Polarization controller
Fiber coupler
Fiber coupler
Detectors
Computer
Dual balanced receiver
Band-pass filter
G1
L1
O1
Diffraction grating
O2
G2
L2
Glass capillary

Fig. 3

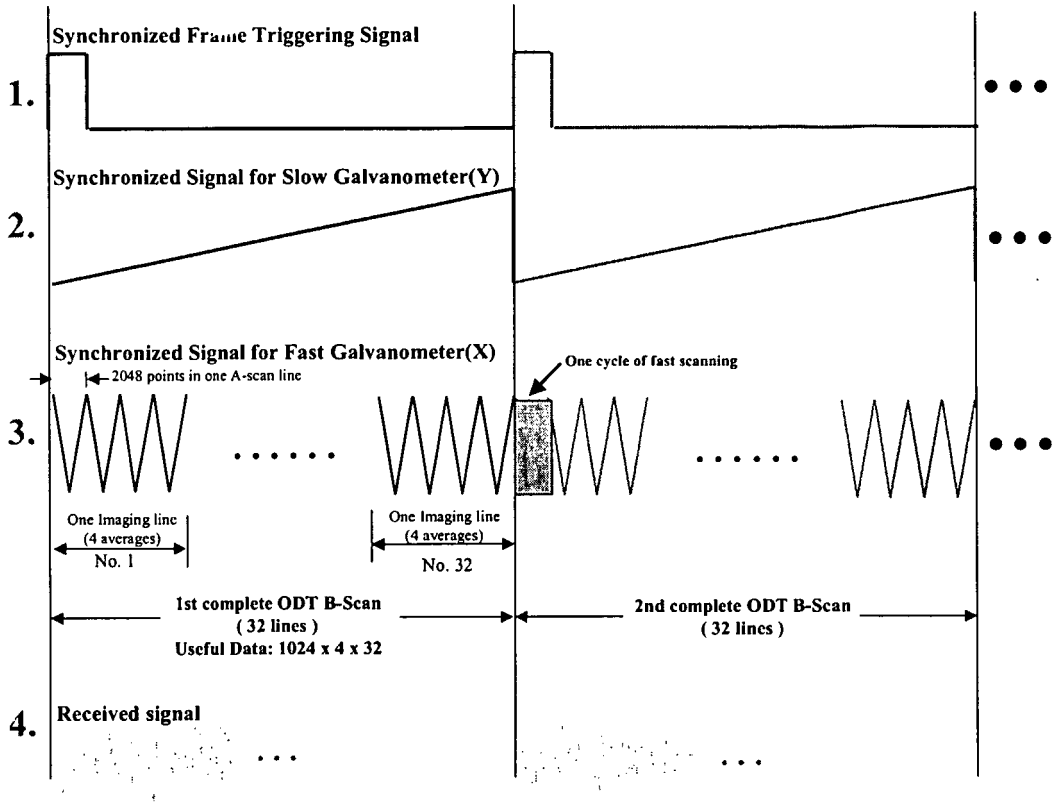
1.
Synchronized Frame Triggering Signal
2.
Synchronized Signal for Slow Galvanometer(Y)
3.
Synchronized Signal for Fast Galvanometer(X)
2048 points in one A-scan line
One cycle of fast scanning
One Imaging line
(4 averages)
No. 1
One Imaging line
(4 averages)
No. 32
1st complete ODT B-Scan
(32 lines)
Useful Data: 1024 x 4 x 32
2nd complete ODT B-Scan
(32 lines)
4.
Received signal

Fig. 4

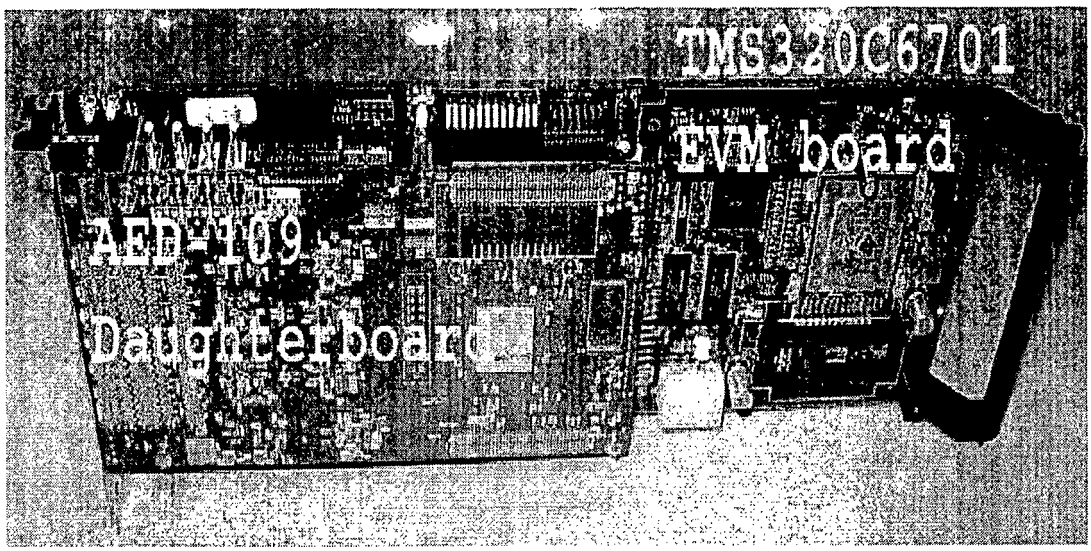

Fig. 5

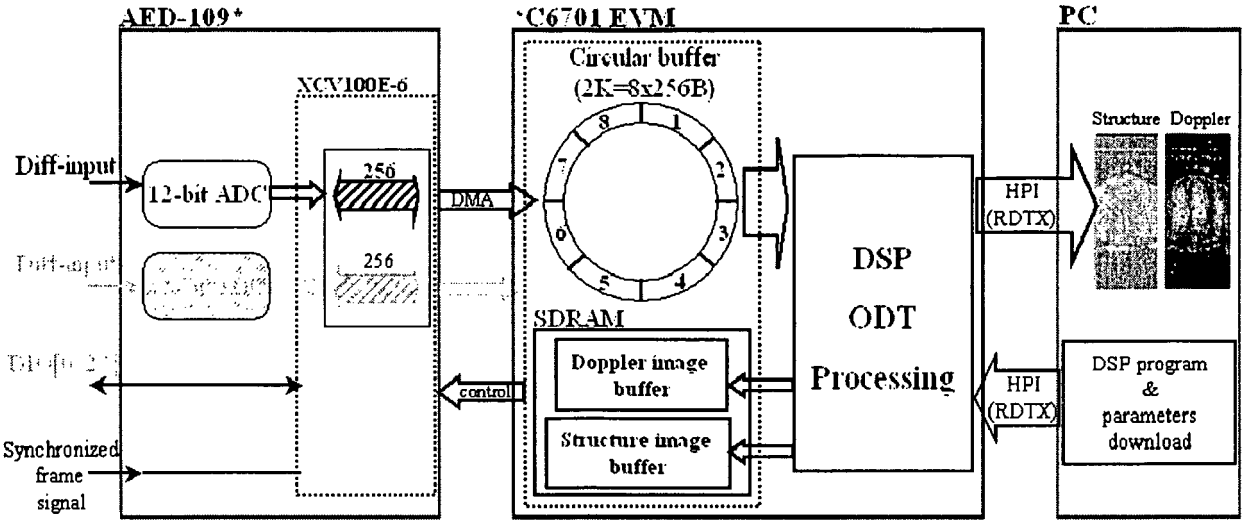
AED-109*
XCV100E-6
Diff-input
12-bit ADC
256
256
DMA
Synchronized frame signal
control
C6701 EVM
Circular buffer (2K=8x256B)
SDRAM
Doppler image buffer
Structure image buffer
DSP ODT Processing
HPI (RDTX)
HPI (RDTX)
PC
Structure
Doppler
DSP program & parameters download

Fig. 6

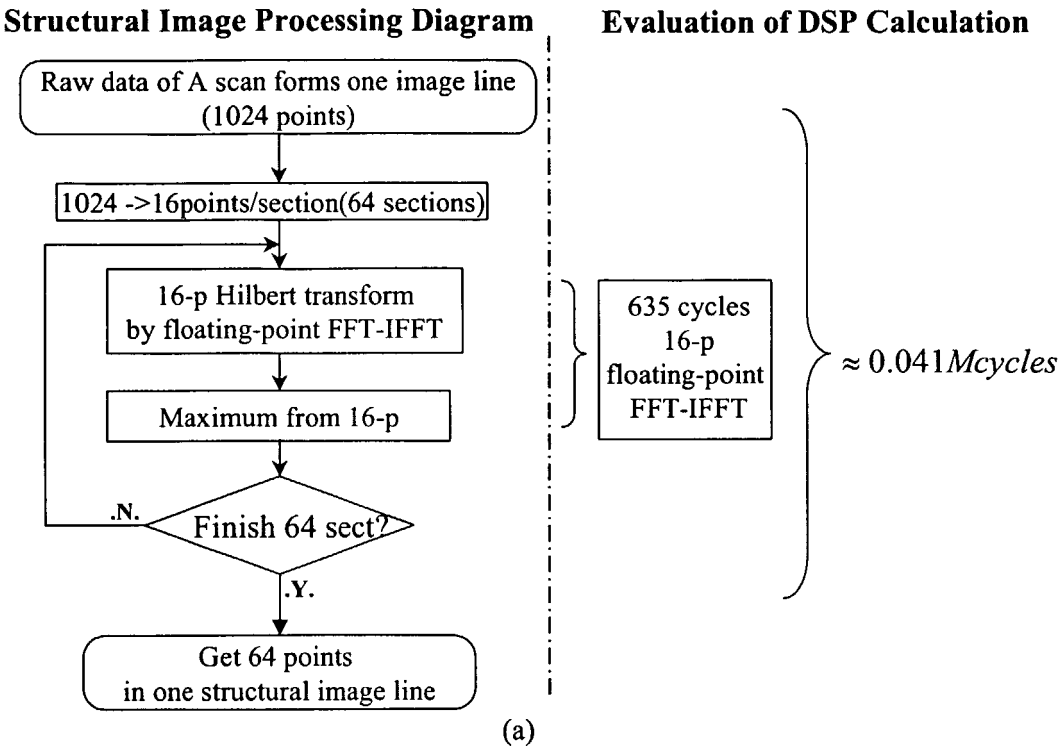
Structural Image Processing Diagram
Evaluation of DSP Calculation
Raw data of A scan forms one image line (1024 points)
1024 ->16points/section(64 sections)
16-p Hilbert transform by floating-point FFT-IFFT
Maximum from 16-p
.N.
Finish 64 sect?
.Y.
Get 64 points in one structural image line
635 cycles 16-p floating-point FFT-IFFT
≈ 0.041Mcycles

(a)

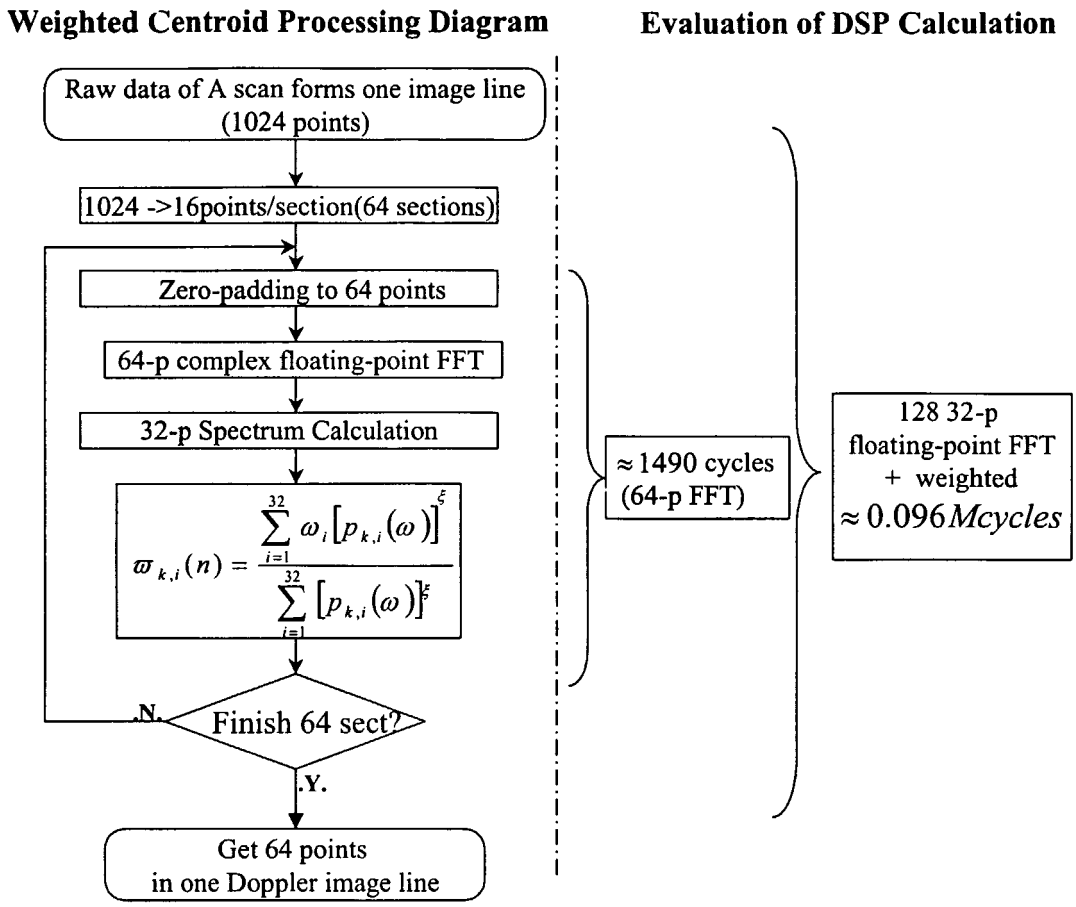
Weighted Centroid Processing Diagram
Evaluation of DSP Calculation
Raw data of A scan forms one image line (1024 points)
1024 ->16points/section(64 sections)
Zero-padding to 64 points
64-p complex floating-point FFT
32-p Spectrum Calculation
$\varpi_{k,i}(n) = \frac{\sum_{i=1}^{32} \omega_i [p_{k,i}(\omega)]^{\xi}}{\sum_{i=1}^{32} [p_{k,i}(\omega)]^{\xi}}$
Finish 64 sect?
.N.
.Y.
Get 64 points in one Doppler image line
≈1490 cycles (64-p FFT)
128 32-p floating-point FFT + weighted
≈ 0.096Mcycles

(b)

Sliding-window Filtering Processing Diagram Evaluation of DSP Calculation

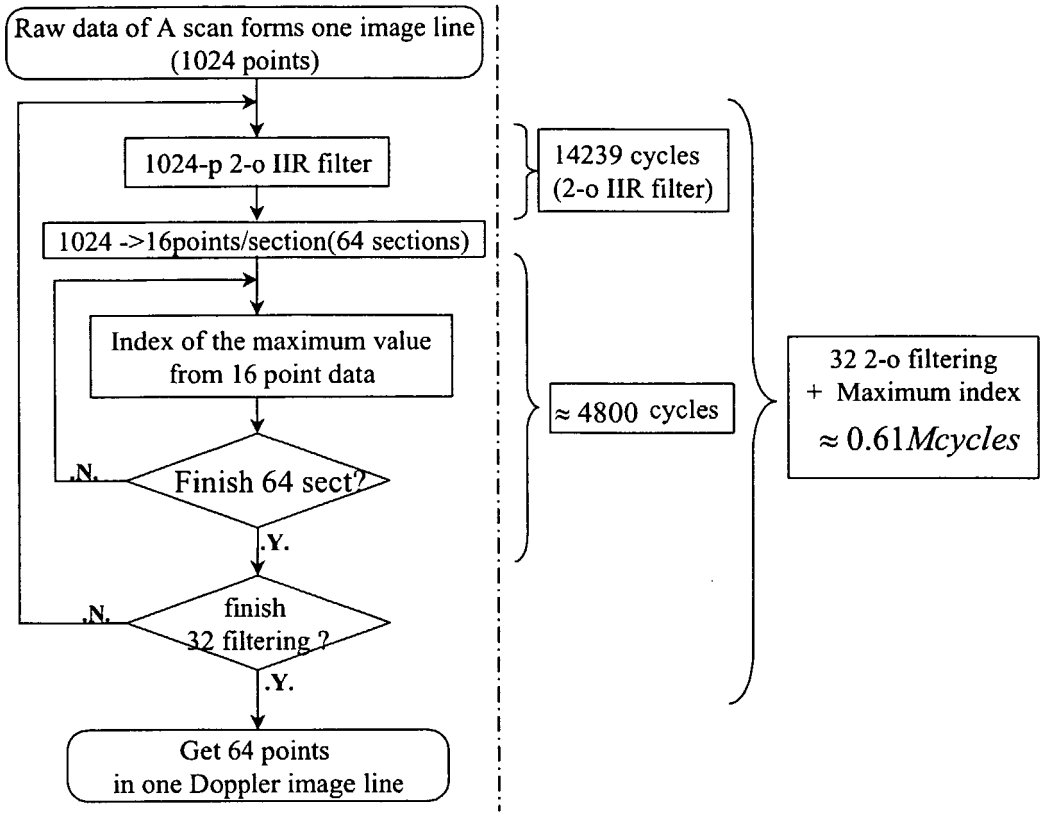

(c)

Fig. 7

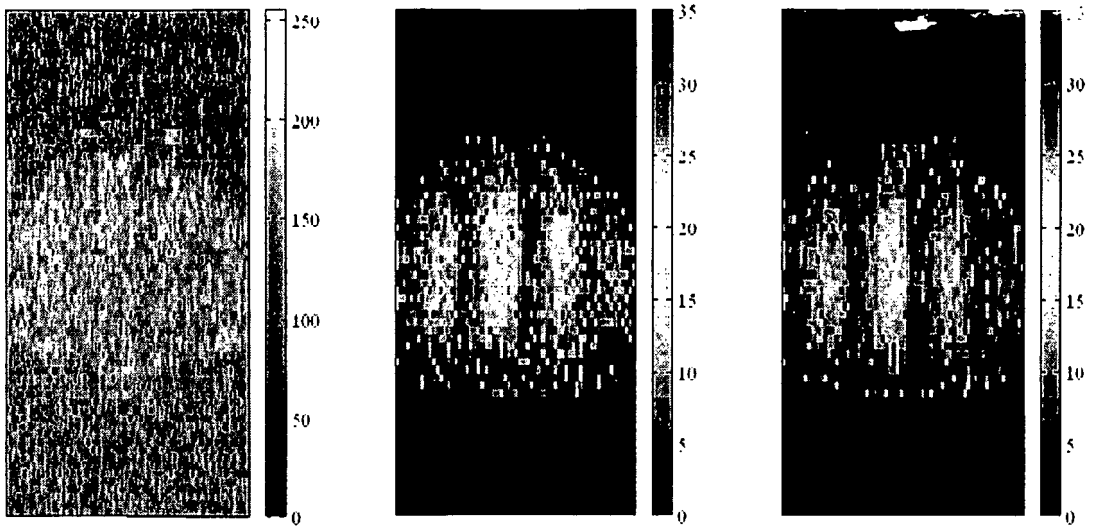

Structural image Weighted centroid image Sliding-window filtering image

(a)

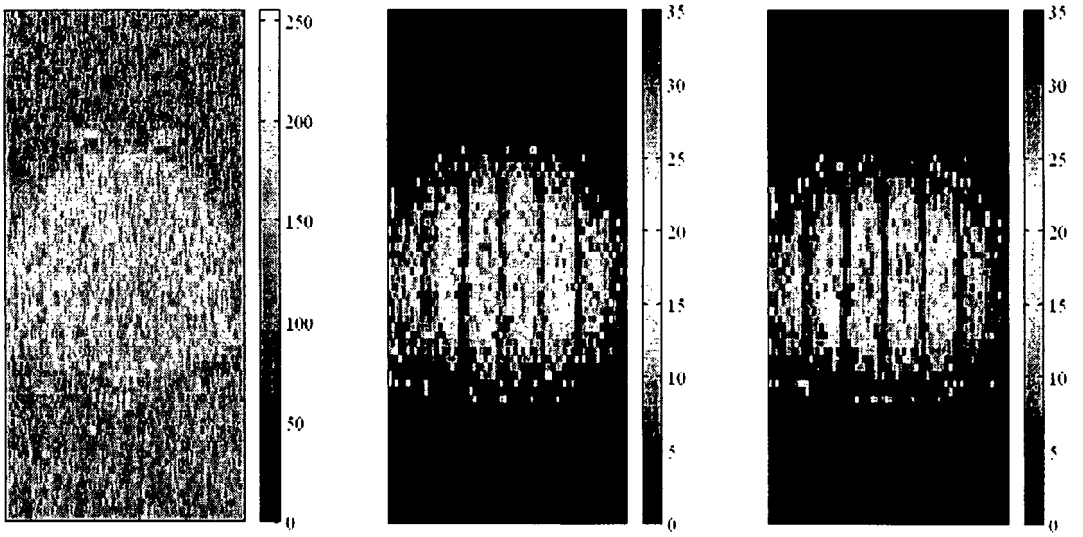

Structural image Weighted centroid image Sliding-window filtering image

(b)

Fig. 8

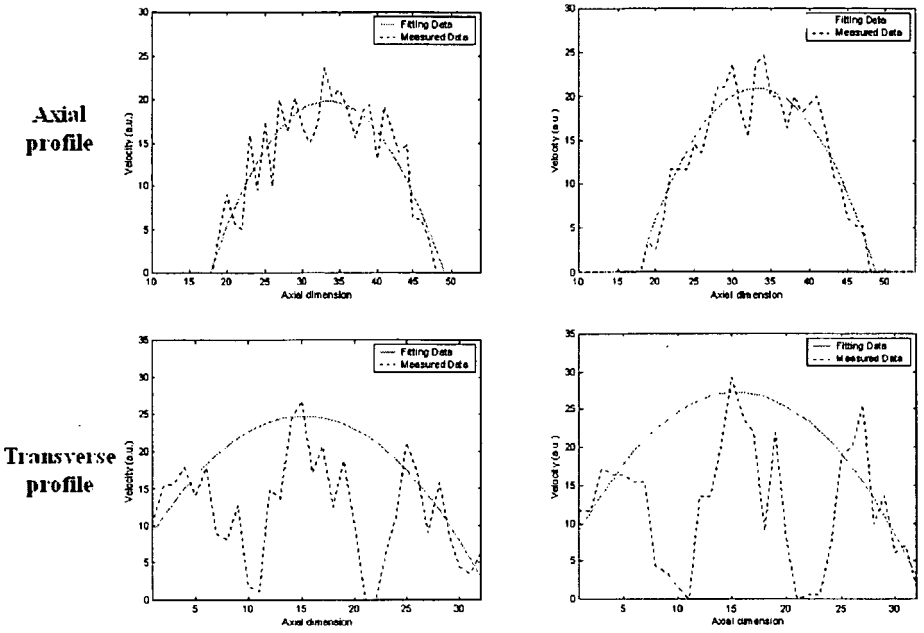

Weighted centroid algorithm Sliding-window filtering algorithm

(a)

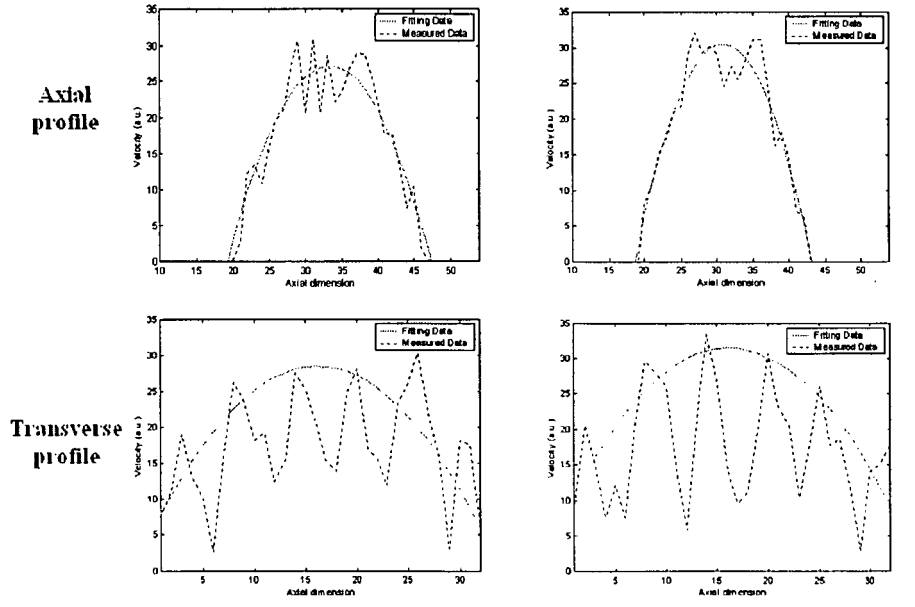

Weighted centroid algorithm Sliding-window filtering algorithm

(b)

Fig. 9

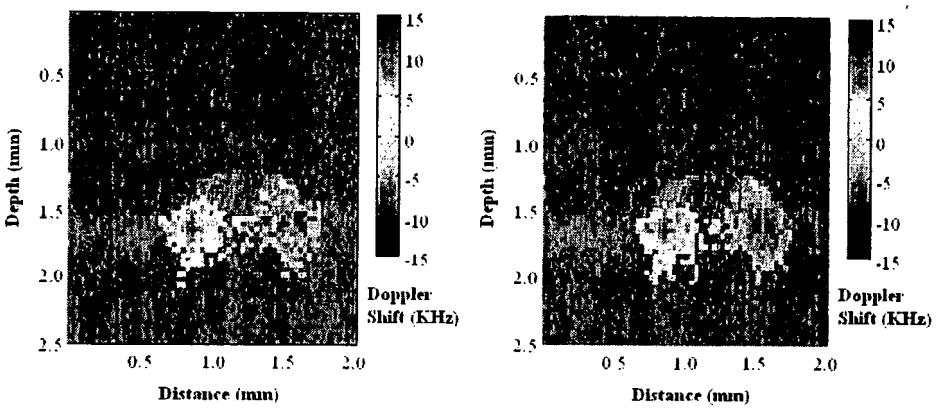

Weighted centroid algorithm **Sliding-window filtering algorithm**

(a) (b)

Fig. 10

INTERNATIONAL SEARCH REPORT

International application No.
PCT/US03/25396

A. CLASSIFICATION OF SUBJECT MATTER

IPC(7) : A 61B 5/05
US CL : 600/476, 473, 425, 427, 431, 436

According to International Patent Classification (IPC) or to both national classification and IPC

B. FIELDS SEARCHED

Minimum documentation searched (classification system followed by classification symbols)
U.S. : 600/476, 473, 425, 427, 431, 436

Documentation searched other than minimum documentation to the extent that such documents are included in the fields searched

Electronic data base consulted during the international search (name of data base and, where practicable, search terms used)

C. DOCUMENTS CONSIDERED TO BE RELEVANT

Category *	Citation of document, with indication, where appropriate, of the relevant passages	Relevant to claim No.
A, P	US 6 485 413 B1 (BOPPART et al.) 26 November 2002, see entire document.	1-19

☐ Further documents are listed in the continuation of Box C. ☐ See patent family annex.

* Special categories of cited documents:

"A" document defining the general state of the art which is not considered to be of particular relevance

"E" earlier application or patent published on or after the international filing date

"L" document which may throw doubts on priority claim(s) or which is cited to establish the publication date of another citation or other special reason (as specified)

"O" document referring to an oral disclosure, use, exhibition or other means

"P" document published prior to the international filing date but later than the priority date claimed

"T" later document published after the international filing date or priority date and not in conflict with the application but cited to understand the principle or theory underlying the invention

"X" document of particular relevance; the claimed invention cannot be considered novel or cannot be considered to involve an inventive step when the document is taken alone

"Y" document of particular relevance; the claimed invention cannot be considered to involve an inventive step when the document is combined with one or more other such documents, such combination being obvious to a person skilled in the art

"&" document member of the same patent family

Date of the actual completion of the international search
23 December 2003 (23.12.2003)

Date of mailing of the international search report
29 DEC 2003

Name and mailing address of the ISA/US
Mail Stop PCT, Attn: ISA/US
Commissioner for Patents
P.O. Box 1450
Alexandria, Virginia 22313-1450
Facsimile No. (703)305-3230

Authorized officer
Dennis W. Ruhl
Telephone No. (703) 308-0858

Form PCT/ISA/210 (second sheet) (July 1998)

专利名称(译)	混合oct /闪烁扫描血管内装置		
公开(公告)号	EP1534128A1	公开(公告)日	2005-06-01
申请号	EP2003788454	申请日	2003-08-14
[标]申请(专利权)人(译)	耶鲁大学		
申请(专利权)人(译)	耶鲁大学		
当前申请(专利权)人(译)	耶鲁大学		
[标]发明人	SINUSAS ALBERT J ZHU QUING SADEGHI MEHRAN M		
发明人	SINUSAS, ALBERT, J. ZHU, QUING SADEGHI, MEHRAN, M.		
IPC分类号	A61B5/00 A61B6/00 A61B5/05		
CPC分类号	A61B5/6852 A61B5/0035 A61B5/0066 A61B6/4057 A61B6/425 A61B6/4258 A61B6/5247		
代理机构(译)	哈利，STEPHEN		
优先权	60/403527 2002-08-15 US		
外部链接	Espacenet		

摘要(译)

成像装置包括形状和尺寸适于进入预定体腔或腔的输送装置，连接到输送装置的OCT系统和连接到输送装置的核成像系统。成像装置还包括连接到OCT系统和核成像系统的控制组件。控制组件包括处理装置，其适于从OCT系统和核成像系统收集信息，并产生用于评估输送装置所放置的体腔或管腔的成像信息。